Draft version August 1, 2014
Preprint typeset using LaTeX style emulateapj v. 5/2/11

SELF-SUSTAINED ASYMMETRY OF LEPTON-NUMBER EMISSION: A NEW PHENOMENON DURING THE SUPERNOVA SHOCK-ACCRETION PHASE IN THREE DIMENSIONS

Irene Tamborra[1 *], Florian Hanke[2,3], Hans-Thomas Janka[2], Bernhard Müller[2 **], Georg G. Raffelt[1], and Andreas Marek[4]
[1] Max-Planck-Institut für Physik (Werner-Heisenberg-Institut), Föhringer Ring 6, 80805 München, Germany
[2] Max-Planck-Institut für Astrophysik, Karl-Schwarzschild-Str. 1, 85748 Garching, Germany
[3] Physik Department, Technische Universität München, James-Franck-Str. 1, 85748 Garching, Germany
[4] Rechenzentrum der Max-Planck-Gesellschaft, Boltzmannstr. 2, 85741 Garching, Germany
Draft version August 1, 2014

ABSTRACT

During the stalled-shock phase of our three-dimensional, hydrodynamical core-collapse simulations with energy-dependent, three-flavor neutrino transport, the lepton-number flux (ν_e minus $\bar{\nu}_e$) emerges predominantly in one hemisphere. This novel, spherical-symmetry breaking neutrino-hydrodynamical instability is termed LESA for "Lepton-number Emission Self-sustained Asymmetry." While the individual ν_e and $\bar{\nu}_e$ fluxes show a pronounced dipole pattern, the heavy-flavor neutrino fluxes and the overall luminosity are almost spherically symmetric. Initially, LESA seems to develop stochastically from convective fluctuations. It exists for hundreds of milliseconds or more and persists during violent shock sloshing associated with the standing accretion shock instability. The ν_e minus $\bar{\nu}_e$ flux asymmetry originates predominantly below the neutrinosphere in a region of pronounced proto-neutron star (PNS) convection, which is stronger in the hemisphere of enhanced lepton-number flux. On this side of the PNS, the mass-accretion rate of lepton-rich matter is larger, amplifying the lepton-emission asymmetry, because the spherical stellar infall deflects on a dipolar deformation of the stalled shock. The increased shock radius in the hemisphere of less mass accretion and minimal lepton-number flux ($\bar{\nu}_e$ flux maximum) is sustained by stronger convection on this side, which is boosted by stronger neutrino heating due to $\langle\epsilon_{\bar{\nu}_e}\rangle > \langle\epsilon_{\nu_e}\rangle$. Asymmetric heating thus supports the global deformation despite extremely nonstationary convective overturn behind the shock. While these different elements of the LESA phenomenon form a consistent picture, a full understanding remains elusive at present. There may be important implications for neutrino-flavor oscillations, the neutron-to-proton ratio in the neutrino-heated supernova ejecta, and neutron-star kicks, which remain to be explored.

Subject headings: supernovae: general — hydrodynamics — instabilities — neutrinos

1. INTRODUCTION

Nonradial hydrodynamic instabilities play an important role in the postbounce dynamics of collapsing stellar cores on their way to the onset of supernova (SN) explosions. They also accompany the formation and cooling of the proto-neutron star (PNS). These phenomena include convection in the PNS, large-scale convective overturn below the stalled shock wave during the accretion-shock phase, and the standing accretion shock instability (SASI). We presently add a new phenomenon to this list which we call LESA for "Lepton-number Emission Self-sustained Asymmetry." Its most conspicuous manifestation is lepton-number flux (ν_e minus $\bar{\nu}_e$) emission primarily in one hemisphere, but it also involves dipolar asymmetry of convection inside the PNS and different strengths of large-scale convective overturn below the stalled shock in both hemispheres.

We first recall these traditional spherical-symmetry breaking instabilities and begin with convection. Prompt post-shock convection leads to the decay of the negative entropy and electron-number gradients left behind by the weakening bounce shock and the shock-breakout burst of electron neutrinos, respectively (Burrows & Fryxell 1992; Janka & Müller 1993; Müller & Janka 1994). It fosters shock expansion and acts as a source of gravitational-wave emission for a period of some ten milliseconds after core bounce (Müller & Janka 1997; Müller, Janka, & Marek 2013). Inside the nascent neutron star (NS), i.e. below (and possibly also around) the neutrinosphere, Ledoux convection was expected to occur because of the negative lepton number gradient produced by the inward progression of the deleptonization wave associated with neutrino losses (Epstein 1979; Burrows & Lattimer 1988). In two-dimensional (2D) simulations (axial symmetry), PNS convection was first studied by Keil, Janka, & Müller (1996) and later again by Buras et al. (2006a) and Dessart et al. (2006).

Large-scale convective overturn below the stalled shock was predicted by Bethe (1990) and confirmed by the first 2D hydrodynamical simulations (Herant, Benz, & Colgate 1992; Herant et al. 1994; Burrows, Hayes, & Fryxell 1995; Miller, Wilson, & Mayle 1993; Janka & Müller 1995, 1996; Mezzacappa et al. 1998) as well as in 3D (Fryer & Warren 2002, 2004). The driving force is a negative entropy gradient that develops a few tens of milliseconds after core bounce in the neutrino-heating region between the gain radius (where neutrino heating begins to exceed neutrino cooling) and the stalled shock. Convective flows stretch the dwelling time of matter in the gain layer and thus increase the energy deposition by neutrinos. This effect can provide crucial support to the delayed neutrino-heating mechanism: multi-D simulations can yield explosions even when spherically symmetric models fail (e.g., Janka & Müller 1996; Murphy & Burrows 2008; Nordhaus et al. 2010a; Hanke et al. 2012; Dolence et al. 2013; Couch 2013; Couch & O'Connor 2014).

* Present address: GRAPPA Institute, University of Amsterdam, Science Park 904, 1098 XH Amsterdam, The Netherlands
** Present address: Monash Center for Astrophysics, School of Mathematical Sciences, Building 28, Monash University, Victoria 3800, Australia

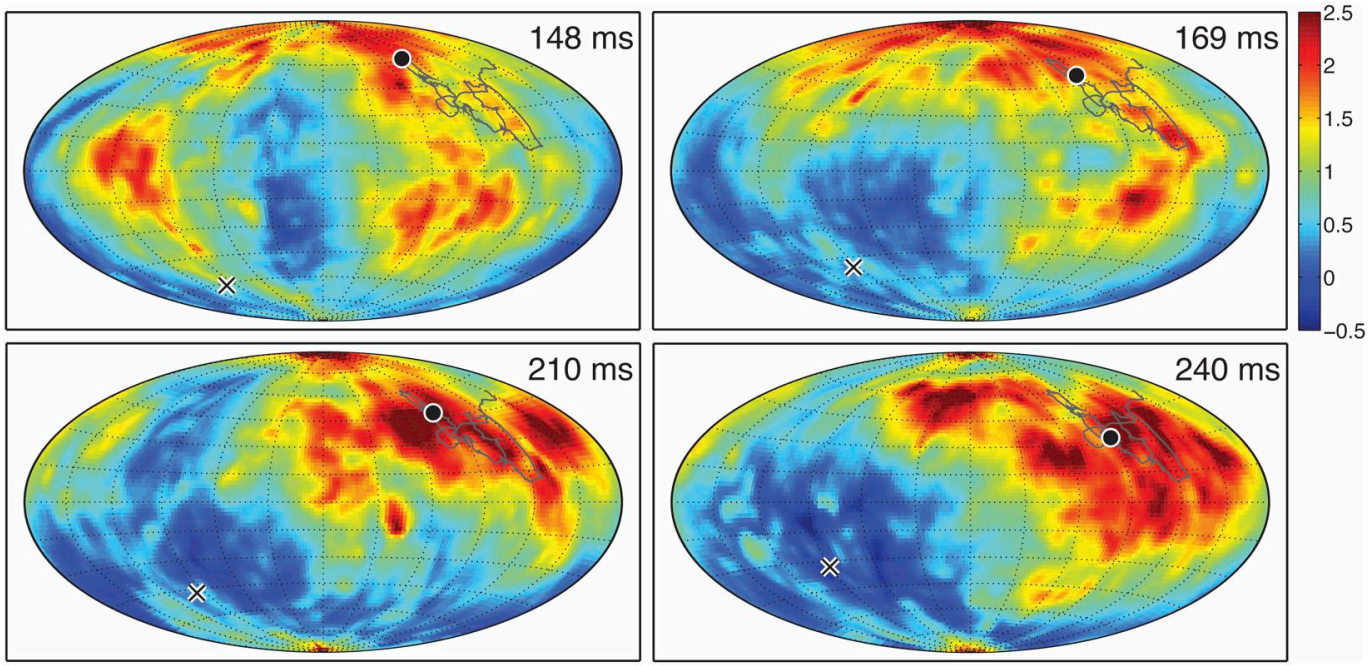

Figure 1. Lepton-number flux (ν_e minus $\bar{\nu}_e$) for our 11.2 $M_\odot$ model as a function of direction for the indicated times post bounce. The latitudes and longitudes, indicated by dotted lines, correspond to the angular coordinates of the polar grid of the numerical simulation. The flux in each panel is normalized to its average, i.e., the quantity $(F_{\nu_e} - F_{\bar{\nu}_e})/\langle F_{\nu_e} - F_{\bar{\nu}_e}\rangle$ is color coded. The lepton-number emission asymmetry is a large-scale feature, which at later times has clear dipole character. The black dots indicate the positive dipole direction of the flux distribution, the black crosses mark the negative dipole direction. The dipole track between 70 and 340 ms is shown as a dark-gray line. Once the dipole is strongly developed, its direction remains essentially stable and shows no correlation with the *x*-, *y*-, and *z*-axes of the numerical grid. The dipole direction is also independent of polar hot spots, which are persistent, local features of moderate amplitude and an artifact connected with numerical peculiarities near the z-axis as coordinate singularity of the polar grid.

The delayed-explosion mechanism is also aided by SASI, which leads to violent shock sloshing motions. This effect expands the shock, increases the gain layer and, again, can enhance the efficiency of neutrino-energy deposition (Marek & Janka 2009) even when convection is weak or its growth is suppressed because of a small shock-stagnation radius and correspondingly fast infall velocities in the gain layer (Foglizzo, Scheck, & Janka 2006; Scheck et al. 2008). This nonradial instability was first observed in 2D simulations with a full 180° grid (Janka & Müller 1996; Mezzacappa et al. 1998; Janka et al. 2003, 2004), but not immediately recognized as a new effect beyond large-scale convection. It was unambiguously identified in 2D hydrodynamical simulations of idealized, adiabatic (and thus non-convective) postshock accretion flows (Blondin, Mezzacappa, & DeMarino 2003). SASI was found to possess the highest growth rates for the lowest-order (dipole and quadrupole) spherical harmonics (Blondin & Mezzacappa 2006; Foglizzo et al. 2007; Iwakami et al. 2008) and to give rise to spiral-mode mass motions in 3D simulations (Blondin & Mezzacappa 2007; Iwakami et al. 2009; Fernández 2010; Hanke et al. 2013) or in 2D setups without the constraint of axisymmetry (Blondin & Mezzacappa 2007; Yamasaki & Foglizzo 2008; Foglizzo et al. 2012). The instability can be explained by an advective-acoustic cycle of amplifying entropy and vorticity perturbations in the cavity between accretion shock and PNS surface (Foglizzo 2002; Foglizzo et al. 2007; Scheck et al. 2008; Guilet & Foglizzo 2012) and has important consequences for NS kicks (Scheck et al. 2004, 2006; Nordhaus et al. 2010b, 2012; Wongwathanarat, Janka, & Müller 2010, 2013) and spins (Blondin & Mezzacappa 2007; Rantsiou et al. 2011; Guilet & Fernández 2013), quasi-periodic neutrino emission modulations (Marek, Janka, & Müller 2009; Lund et al. 2010; Tamborra et al. 2013), and SN gravitational-wave signals (Marek, Janka, & Müller 2009; Murphy, Ott, & Burrows 2009; Müller, Janka, & Marek 2013).

Here we report the discovery of a new type of low-mode nonradial instability, LESA, which we have observed in 3D hydrodynamical simulations with detailed, energy-dependent, three-flavor neutrino transport using the Prometheus-Vertex code. Our current portfolio of simulated 3D models includes an 11.2 $M_\odot$ model that shows violent large-scale convection, but no obvious signs of SASI activity during the simulated period of postbounce evolution, and two models (20 $M_\odot$ and 27 $M_\odot$) in which episodes of SASI alternate with phases of dominant large-scale convection (Hanke et al. 2013; Tamborra et al. 2013, 2014). While all models exhibit LESA, with different orientations of the emission dipole, the clearest case is the 11.2 $M_\odot$ model, because the new effect is not overlaid with SASI activity.

To provide a first impression of our new and intriguing phenomenon we show in Fig. 1 the distribution of lepton-number emission (ν_e minus $\bar{\nu}_e$) for the 11.2 $M_\odot$ model over the stellar surface at postbounce (p.b.) times of 148, 169, 210, and 240 ms. In each panel, the lepton-number flux is normalized to the instantaneous average and the color scale covers the range from −0.5 to 2.5 of this relative measure. We indicate the positive dipole direction with a black dot, the negative direction with a cross. We also show the track of the positive dipole direction as a dark-gray line, ranging from 70 ms p.b., where the dipole begins forming, to the end of the simulation at 340 ms. While at 148 ms the dipole pattern is not yet strong—a quadrupole component is clearly visible and the dipole is still building up as we will see later—the subse-

quent snapshots reveal a strong dipole pattern with large amplitude: In the negative-dipole direction, the lepton-number flux is around zero, and even negative in some small regions, whereas in the positive direction it is roughly twice the average and even larger in some small regions.

LESA is a large and conspicuous effect concerning the deleptonization flux. At the same time, it is associated with more subtle dipole deformations of other quantities. In particular, the dipolar lepton-number emission is linked to anisotropic PNS convection, which leads to an aspherical electron distribution in the PNS mantle layer. The emission dipole is additionally fed by a hemispheric mass-accretion asymmetry, which might cause the one-sided enhancement of PNS convection. This accretion asymmetry in turn is a consequence of a dipolar shock deformation that deflects the accretion flow preferentially to one hemisphere. Despite vigorous and highly time-variable, nonstationary convective overturn stirring the postshock region, the shock deformation and mass-accretion asymmetry are maintained for hundreds of milliseconds by a neutrino-heating asymmetry that is tightly linked to the neutrino-emission anisotropy: Because $\bar{\nu}_e$ have somewhat harder spectra than ν_e, neutrino heating on the side of a relatively higher $\bar{\nu}_e$ flux (the side with lowest lepton-number flux and lowest mass accretion rate) is stronger and sustains the dipolar shock deformation that produces the hemispheric asymmetry of the postshock accretion flow.

This preliminary interpretation suggests that LESA is not a purely hydrodynamical phenomenon, in contrast to the traditional instabilities, but depends on a complex interaction of hydrodynamic mass flow and neutrino emission and heating.

Our new effect is predominantly a hemispheric asymmetry in these quantities and as such is not a generic 3D effect, but it has not been previously reported in the context of 2D simulations. Actually, indications of LESA may be present in the O-Ne-Mg core explosions of Wanajo, Janka, & Müller (2011) and in a $15\,M_\odot$ explosion model of Müller et al. (2012b). However, it seems difficult to make a strong case for this neutrino-hydrodynamical instability based on 2D simulations. The constraint of axisymmetry resticts any dipole asymmetry to the direction of the polar axis of the grid. This symmetry axis, where reflecting boundary conditions are imposed, defines a preferred direction and has various problematic consequences. It tends to artificially create hemispheric differences by deflecting the converging flows either inward or outward, and the grid axis also directs shock-sloshing motions. Strong bipolar motions of the postshock accretion layer in most 2D simulations, where shock expansion and contraction alternate violently between the poles, could interfere with the LESA phenomenon or even create asymmetries of different nature.

In the following, we first describe briefly, in Sect. 2, the numerical setup of our 3D simulations and the overall properties of our three progenitor models. In Sect. 3 we study various manifestations of our new phenomenon, ranging from dipole deformations of neutrino-emission properties to asymmetric PNS convection. Next we turn in Sect. 4 to more subtle manifestations in the form of asymmetric accretion and neutrino heating, which however form a feedback loop and as such are the driving engine of the overall effect. In Sect. 5 we string the different elements together and provide an overall scenario that involves the outer feedback mechanism consisting of asymmetric mass accretion and neutrino heating and the inner mechanism of asymmetric electron-density distribution and PNS convection. We conclude in Sect. 6 with a summary and a discussion of possible implications.

2. NUMERICAL 3D MODELS

The calculations of our 3D models were performed with the elaborate neutrino-hydrodynamics code Prometheus-Vertex. This SN simulation tool combines the hydrodynamics solver Prometheus (Fryxell et al. 1989), which is a dimensionally-split implementation of the piecewise parabolic method (PPM) of Colella & Woodward (1984), with the neutrino transport module Vertex (Rampp & Janka 2002). Vertex solves the fully energy-dependent moment equations for the neutrino energy and momentum densities, with $O(v/c)$ velocity dependence, for spherically symmetric transport problems defined to be associated with every angular bin of the polar grid ("radial rays") used for the multi-dimensional simulations. The moment equations are closed by a variable Eddington factor relation that is provided by the formal solution of a model Boltzmann equation. An up-to-date set of neutrino interaction rates is applied in Vertex (see, e.g., Müller et al. 2012b). In the multi-dimensional case, our "ray-by-ray-plus" approach (Buras et al. 2006b) includes non-radial neutrino advection and pressure terms in addition to the radial transport solves. The ray-by-ray approximation implies that we assume the neutrino radiation field to be axially symmetric around the radial direction and thus ignore nonradial components of the neutrino flux. In the simulations presented here, we adopted monopolar gravity but included general relativistic corrections by means of an effective gravitational potential (Marek et al. 2006).

We have performed 3D simulations for the evolution of the $11.2\,M_\odot$ and $27\,M_\odot$ progenitors of Woosley et al. (2002) and the $20\,M_\odot$ model of Woosley & Heger (2007), using the high-density equation of state (EoS) of Lattimer & Swesty (1991) with a nuclear incompressibility of $K = 220$ MeV. The $11.2\,M_\odot$ and $27\,M_\odot$ stars had been previously investigated in 2D by Buras et al. (2006a), Marek & Janka (2009), Müller et al. (2012b), and Müller et al. (2012a). Our 3D models were computed on a spherical polar grid with an initial resolution of $n_r \times n_\theta \times n_\phi = 400 \times 88 \times 176$ zones. Later, refinements of the radial grid ensured adequate resolution in the PNS surface region. The innermost 10 km were treated in spherical symmetry to avoid excessive time-step limitations near the polar grid axis. Doing so we took special care to ensure that the convectively unstable layer below the neutrinosphere and the corresponding undershooting region were fully covered by the 3D grid during the entire simulations. Seed perturbations for aspherical instabilities were imposed by hand 10 ms after core bounce by introducing random perturbations of 0.1% in density on the entire computational grid. None of these models led to successful explosions during the simulation periods of 350 ms for the $11.2\,M_\odot$ model, 420 ms for the $20\,M_\odot$ progenitor, and 575 ms for the $27\,M_\odot$ case.

The postbounce hydrodynamics of the $27\,M_\odot$ model, in particular the prominent presence of SASI sloshing and spiral modes, was described in detail in a previous paper (Hanke et al. 2013). Basic properties of the neutrino signal and its detection were subject of a recent paper by Tamborra et al. (2013), highlighting the large-amplitude, quasi-periodic modulations of the radiated luminosities and mean energies associated with the SASI activity. In addition, information about the expected neutrino signal from the $20\,M_\odot$ and $11.2\,M_\odot$ runs was shown. More details on the neutrino emission of all three 3D simulations and implications for the direction dependent detectability of SN neutrino signals will be discussed in Tam-

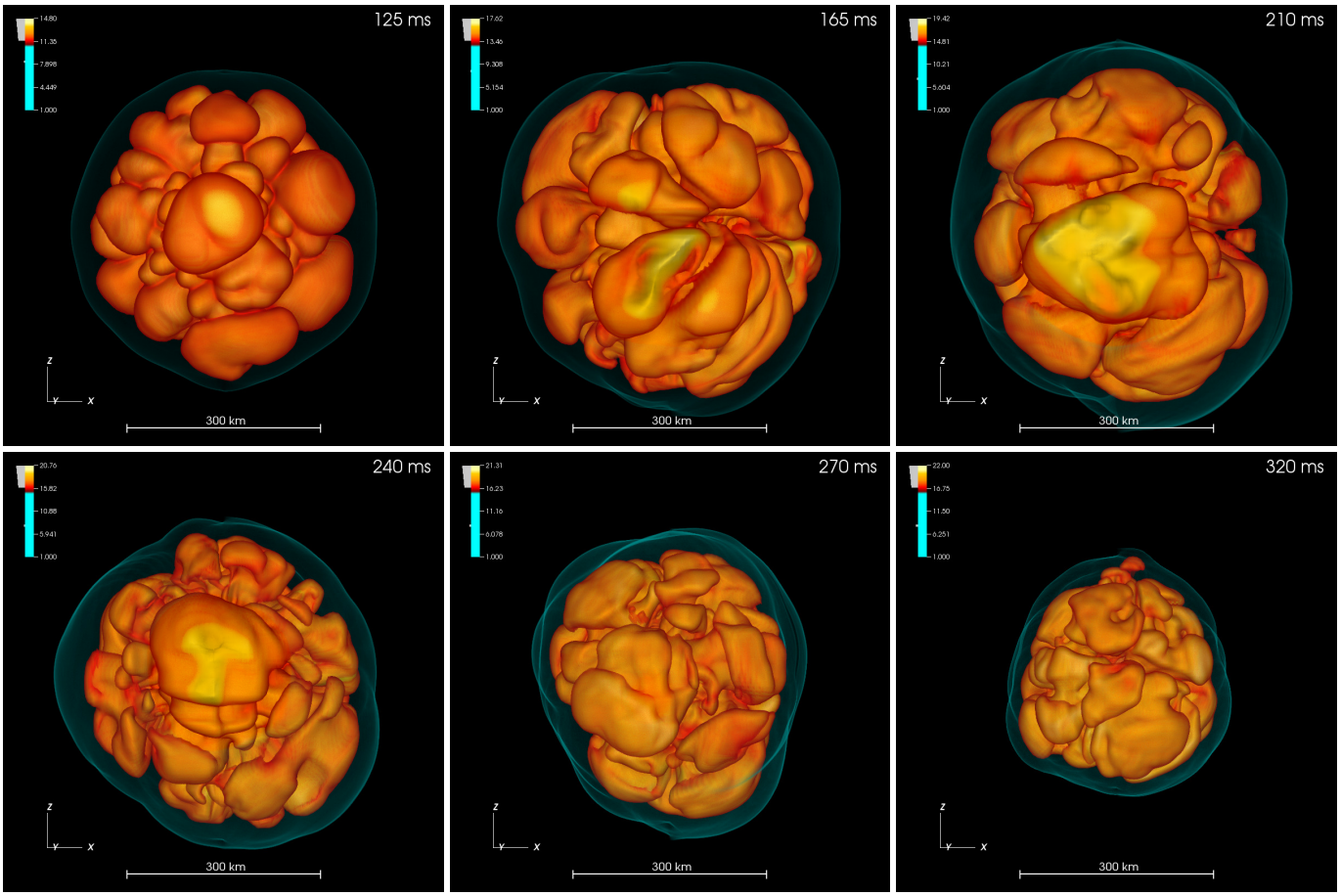

Figure 2. Snapshots of the convective overturn activity during the accretion phase of the 11.2 $M_\odot$ model at the indicated p.b. times. Visualized are surfaces of constant entropy: The bluish, semi-transparent envelope is the SN shock, the red-orange-yellow surfaces are entropy structures in the postshock region. Neutrino-heated high-entropy matter expands in typical mushroom-like, buoyant plumes. These features are highly time dependent with bubbles continuously appearing, expanding and rising, and disappearing to give way to a new generation of convective plumes. The direction of strongest lepton-number emission, i.e., the largest excess of the radiation of ν_e compared to $\bar{\nu}_e$ (see text), points towards the observer, above the x-y-plane at roughly 45° inclination to the z-axis. A corresponding global, persistent dipolar deformation of the accretion shock is present but can hardly be recognized without a detailed analysis.

borra et al. (2014).

The 27 $M_\odot$ and the 20 $M_\odot$ models both show periods of strong SASI activity. In the former case, which was simulated until 575 ms p.b., a first phase of violent SASI occurs between ∼170 ms and ∼260 ms (Hanke et al. 2013), and a second SASI episode sets in at ∼420 ms after an intermediate period of essentially pure convective overturn. In the 20 $M_\odot$ case strong SASI mass motions take place from ∼170 ms until ∼305 ms, and SASI reappears after 400 ms, shortly before the simulation run was stopped. On the other hand, the 11.2 $M_\odot$ model does not exhibit any clear evidence of SASI motions but develops the typical signatures of postshock convective overturn in the neutrino-heating layer as evident from our Fig. 2, to be compared with the 27 $M_\odot$ case in Fig. 1 of Hanke et al. (2013). In the 11.2 $M_\odot$ model, the short-timescale neutrino-emission variations are distinctly smaller than in the SASI-active models (Tamborra et al. 2013, 2014).

In the 11.2 $M_\odot$ simulation, first indications of postshock convection become visible at about 80 ms p.b., shortly after a gain region below the stalled shock has developed. Buoyant, mushroom-like plumes appear, which are initially small and then successively replaced by larger ones. At 100 ms p.b., first evidence of shock deformation occurs, and after about 140 ms, convective overturn has attained its full strength with a ratio of maximum to minimum shock radius of up to $R_{\rm s,max}/R_{\rm s,min} \sim 1.35$. The expansion of the accretion shock continues until about 210 ms p.b., when the average shock radius reaches a maximum of ∼260 km (see Fig. 12 below). It is followed by a slow but monotonic recession of the average shock radius to only 150 km at the end of the simulation at 350 ms. No explosion has set in until this stage, in contrast to the corresponding 2D calculation with the same microphysics, same numerical treatment, and in particular the same radial and angular grid resolution. In the 2D case, the shock continues to expand, supported by large-amplitude shock-sloshing motions along the symmetry axis. More and more favorable conditions for an explosion develop until finally, at roughly 350 ms p.b., the shock accelerates and triggers an outgoing blast wave, whereas the 3D case at this time shows little promise of an explosion.

Apparently, the 3D setup with the chosen angular resolution (limited by the requirements of computational resources, which are prohibitive for our sophisticated treatment of neutrino transport) is less beneficial for the possibility of a SN explosion by the neutrino-driven mechanism. This finding is in line with recent investigations based on cruder treatments of neutrino physics, namely a neutrino-light bulb description with simple heating and cooling terms (Hanke et al. 2012; Couch 2013), ray-by-ray neutrino trapping with a parametrized heating strength (Couch & O'Connor 2014),

and a ray-by-ray implementation of the isotropic diffusion source approximation (Takiwaki, Kotake, & Suwa 2014). However, the difference between 2D and 3D models is not subject of our present discussion and we next turn to the new phenomenon of asymmetric lepton-number emission.

3. PERSISTENT DIPOLE ASYMMETRIES OF 3D MODELS

3.1. *Evolution of lepton-number emission dipole*

We have recently explored the flavor-dependent neutrino emission of our 3D simulations to forecast possible signatures of hydrodynamical instabilities in large-scale neutrino detectors (Tamborra et al. 2013) and as a prerequisite for flavor oscillation studies. A systematic analysis has revealed a long-lasting, slowly evolving dipole asymmetry of the lepton-number (ν_e minus $\bar{\nu}_e$) emission from the newly formed NS. In Fig. 1 we have shown typical directional distributions of the lepton-number flux for our 11.2 $M_\odot$ model. This pronounced asymmetry builds up in parallel to the development of large-scale convective overturn behind the stalled shock and shows a fairly stable direction, which has no particular correlation with the numerical coordinate grid[3].

Before attempting a physical interpretation of this puzzling phenomenon, we first collect a number of conspicuous phenomenological manifestations. A natural first question is to see when and how this effect builds up in the course of postbounce core-collapse evolution and if it is correlated with other symmetry-breaking hydrodynamical instabilities.

To quantify the time evolution of our new effect we consider the lowest-order multipole components of the lepton-number flux as a function of emission direction. To clarify our normalization of the dipole component we note that if the lepton-number flux distribution contains only a monopole and dipole term, then the distribution is $A_{\rm Monopole} + A_{\rm Dipole}\cos\vartheta$ in coordinates aligned with the dipole direction. When the ratio of these amplitudes is unity, the distribution is proportional to $1+\cos\vartheta$ and the lepton-number flux vanishes in the direction of minimal flux and is twice the average in the direction of maximal flux, corresponding roughly to what we see in Fig. 1. $A_{\rm Monopole}$ is nothing but the total rate of lepton number emitted by the evolving PNS, whereas $A_{\rm Dipole}$ is 3 times the projection of the total lepton-number flux onto the dipole direction.

Figure 3 shows the evolution of $A_{\rm Monopole}$ and $A_{\rm Dipole}$ and the dipole direction for our three progenitor models. The total lepton-number emission is at first off-scale, corresponding to the usual prompt ν_e burst, and then decreases monotonically with small modulations caused by large-scale convection and concomitant variations of the postshock accretion flow. The overall lepton-number emission is fed by the mass-accretion flow so that it is not surprising that the monopole strength depends considerably on the progenitor model.

In all models, a dipole component becomes first discernible at about 50 ms p.b., grows for 100–150 ms, and later begins to decrease, more or less in parallel with the overall decline of the lepton-number emission. The dipole decay is not monotonic and has an overall gradient that is different in the different progenitors (steepest in the 11.2 $M_\odot$ model). In this later phase, the dipole amplitude sometimes exceeds the monopole, meaning that in the negative dipole direction, the lepton-number flux is somewhat negative (excess of $\bar{\nu}_e$ over ν_e emission). The overall dipole strength is similar in all three progenitor models, at the peak reaching a value of $\sim$3–4 $\times\,10^{56}$ s^{-1}.

While in all three models the dipole growth sets in and reaches large amplitudes during an early, convection-dominated postbounce phase, before SASI activity starts in the postshock layer, it is remarkable that SASI seems to have different consequences for the LESA evolution in the 20 $M_\odot$ and 27 $M_\odot$ models. In the former case the lepton-number emission dipole continues to grow even after the onset of SASI and reaches its full strength during the SASI-dominated phase. In contrast, in the 27 $M_\odot$ model the onset of SASI seems to prevent a further growth of the dipole amplitude, which instead performs quasi-periodic oscillations around a stable level somewhat below the maximum dipole amplitudes in the 11.2 and 20 $M_\odot$ models. The dipole continues to develop to its peak amplitude only after the SASI episode has ended and convective overturn becomes the dominant hydrodynamic instability in the postshock accretion layer again. We will come back to this interesting difference later in our discussion of the physical elements and underlying physical mechanism of LESA (see Sect. 4.4).

The dipole orientation on the computational polar grid is expressed by latitudinal and azimuthal polar angles θ and ϕ, respectively. The zenith angle, θ, varies from $\pi/2$ (north pole of numerical grid) to $-\pi/2$ (south pole), whereas $-\pi \le \phi \le \pi$ is measured relative to the x-axis of the grid. The dipole direction slowly drifts, but remains fairly stable once the dipole is well developed. This conclusion also follows from the dipole's sky-track shown as a dark-gray line in Fig. 1 for the 11.2 $M_\odot$ case. It is remarkable that this behavior is quite similar in the higher-mass (20 and 27 $M_\odot$) progenitors, where phases with dominant large-scale convection alternate with phases of pronounced SASI activity, which are indicated in Fig. 3 by horizontal bars. The SASI action is clearly visible in the form of small, periodic modulations of the overall deleptonization flow and much larger modulations of the dipole strength and direction with typical oscillation periods of $\sim$10–20 ms. Yet, even these modulations are only relatively small variations of the dipole strength and its orientation in space, not changing the hemispheric location of the whole phenomenon. The initial, large movement of the azimuthal angle from $+180^\circ$ to about -90° that happens between about 90 and 110 ms in the case of the 20 $M_\odot$ model (Fig. 3) occurs in a phase when the dipole is still building up and its amplitude is correspondingly small. Therefore the dipole direction is not particularly meaningful and the step-like jumps of its azimuth angle simply reflect stochastical fluctuations. At later times the dipole orientations in all three models exhibit only very slow drifts.

The lepton-emission dipole is a long-lasting, persistent, and only slowly evolving phenomenon. Its dipole direction remains in the same hemisphere for periods of hundreds of milliseconds, i.e., for nearly the whole computed postbounce evolution. A slow overall drift of the dipole direction (mainly in the 20 and 27 $M_\odot$ models) happens on timescales much longer than the typical dynamical timescales in the convective layers inside the PNS and between the gain radius and stalled shock. With convective velocities of up to a few 10^8 cm s^{-1} in the former case and up to more than 10^9 cm s^{-1} in the latter, convective overturn timescales are typically milliseconds in the PNS and around $\sim$10 ms in the neutrino-heating re-

[3] The orientation of the coordinate system in our sky-plots of Figs. 1, 6, 7, and 8 is such that the north-south direction corresponds to the z-axis of the numerical grid, the center of the plot is the $-x$ direction, and the left and right extreme points correspond to the $+x$ direction. The half-way points on the equator belong to the $+y$ (left) and $-y$ directions.

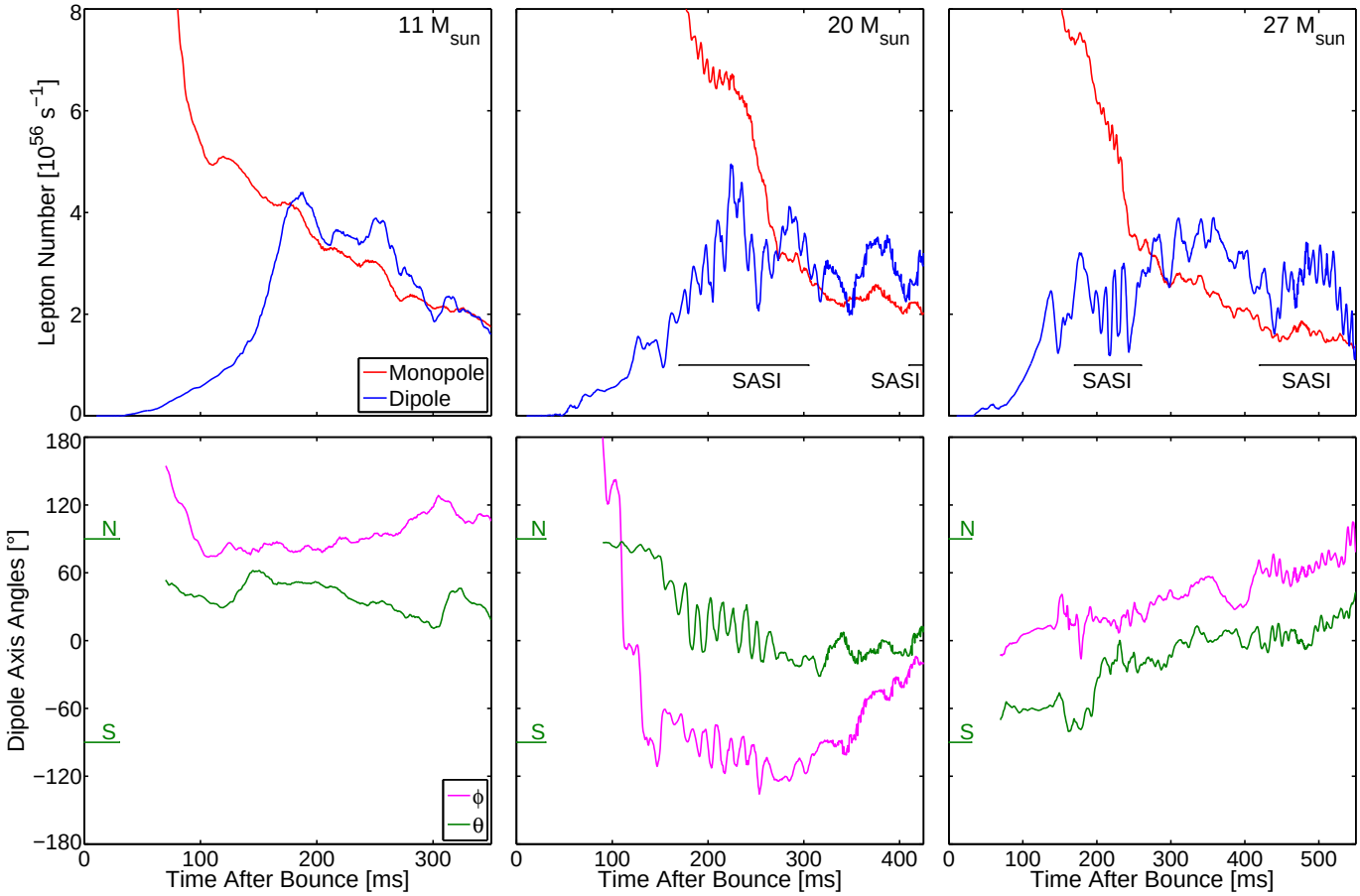

Figure 3. Time evolution of the lepton-number emission (ν_e minus $\bar{\nu}_e$) for the 11.2, 20 and 27 $M_\odot$ models as labelled. For each model, the upper panels show the overall lepton number flux (monopole of the angular distribution; red curve) and its dipole component (blue curve). Episodes of dominant SASI activity are marked by horizontal bars. The lower panels display the zenith angle θ (green line) and the azimuth angle ϕ (magenta line) of the dipole direction, which describes the track shown for the 11.2 $M_\odot$ case in Fig. 1. For the zenith angle we indicate the north- and south-polar grid directions at ±90° on the vertical axis. The monopole evolution depends strongly on the accretion rate and varies between the models, whereas the maximum dipole amplitude is similar in all cases and shows a similar initial growth phase. The dipole persists (and can even grow) during the indicated phases of pronounced SASI activity. The dipole directions are different in all cases, bear no correlation to the numerical grid, and they drift only slowly even during SASI phases.

gion. These timescales depend on the radial diameter of the PNS convection zone (roughly 10 km, which also determines the angular scale of ∼20–40° of convective cells there) and on the shock stagnation radius, respectively. The dynamical timescales of the postshock region are reflected by the SASI-imprinted modulations of dipole strength and spatial orientation visible in Fig. 3. Convective activity in both regions is highly time dependent and nonstationary, and individual convective cells and buoyant bubbles have life times that are usually not much longer than one or two overturns (for PNS convection this was discussed by Keil, Janka, & Müller 1996; Dessart et al. 2006). It is therefore astonishing that despite such an extreme time variability of the environment a hemispheric emission asymmetry can survive over many tens of dynamical periods. Only over long, secular timescales SASI or convectively induced changes of the system seem to lead to a gradual, slow drift of the dipole orientation as seen in all models but especially in those with episodes of vigorous SASI activity (Fig. 3, panels in the middle and right columns).

These simple observations already suggest that the LESA phenomenon must physically depend on a complicated interplay of different effects. The initial growth over 100–150 ms parallels the growth of large-scale convection in the gain region, suggesting gain-region convection as the primary engine. On the other hand, the persistence throughout SASI episodes and the near-universal dipole strength suggest that LESA must also be anchored to deeper regions. We will see that indeed it originates in the PNS convection region deep below the neutrinospheres.

3.2. *Overall neutrino emission properties*

Before turning to physical interpretations, however, we first continue with our description of phenomenological observations in our numerical models. In particular, one may wonder if the overall neutrino emission parameters exhibit any peculiarities, but this is not the case. We specifically show in Fig. 4 the evolution of the overall energy-loss rate for the 11.2 $M_\odot$ model in the three species ν_e, $\bar{\nu}_e$, and ν_x, i.e., we display the 4π-integrated energy fluxes,

$$\dot{E}_\nu(t) \equiv \int_{4\pi} \mathrm{d}\Omega\, R^2 F_\mathrm{e}(\boldsymbol{R}, t)\,, \qquad (1)$$

where $F_\mathrm{e}(\boldsymbol{R}, t)$ is the ray-by-ray computed energy-flux density at a point $\boldsymbol{R}$ of a chosen sphere with radius $R = |\boldsymbol{R}|$. The quantity $\dot{E}_\nu(t)$ is usually called "luminosity" but it is not measurable in the multi-dimensional case by observers at any location. The bottom panel of Fig. 4 shows the corresponding 4π-averaged mean energies, $\langle \epsilon_{\nu_i} \rangle$, which are defined as the ra-

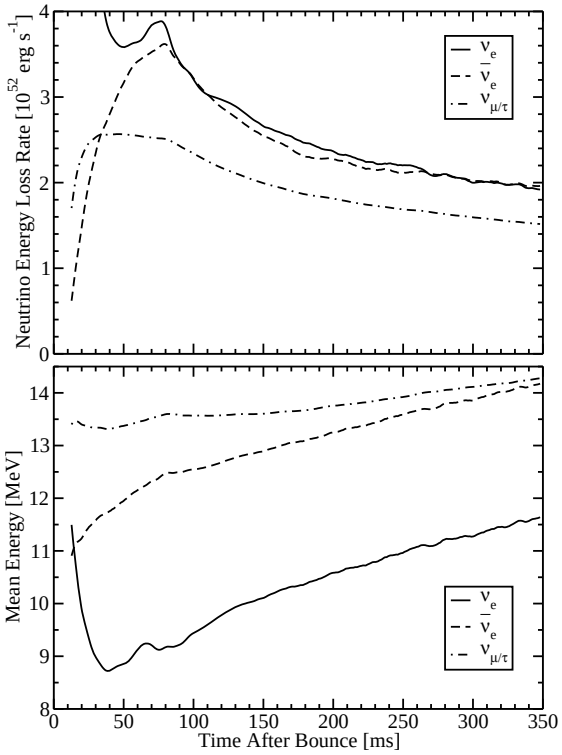

Figure 4. Time evolution of spherically averaged neutrino emission properties (laboratory frame) for the 11.2 $M_\odot$ model. *Top:* Energy loss rates, integrated over all directions, for ν_e, $\bar{\nu}_e$, and (one kind of) ν_x. *Bottom:* Mean energies, averaged over all directions. These results do not show any peculiarities and are similar to comparable 1D and 2D simulations.

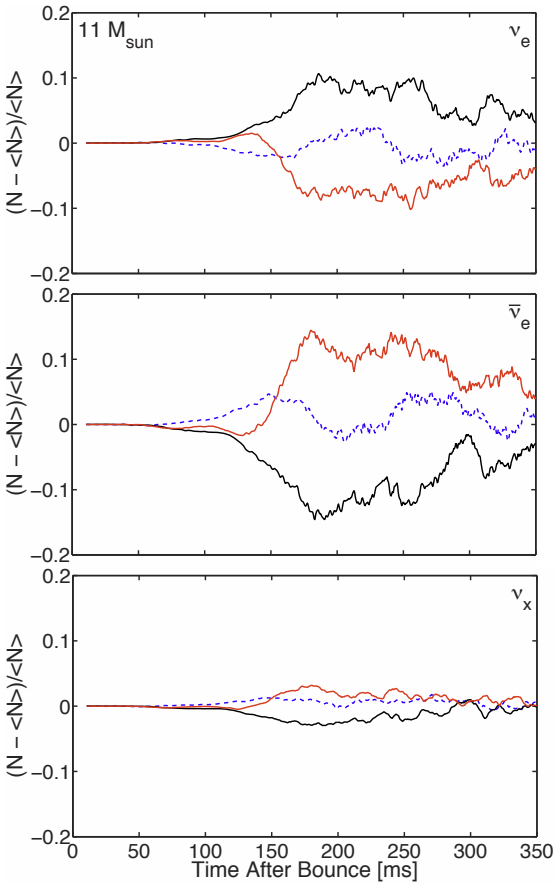

Figure 5. Time evolution of the ν_e, $\bar{\nu}_e$, and heavy-lepton neutrino (ν_x) number fluxes (top to bottom) relative to their directional averages for the 11.2 $M_\odot$ model. We show hemispheric averages (accounting for projection effects; see text) as seen by distant observers who are located approximately in the direction of maximal lepton-number emission (black), in the opposite direction (red) and in a representative transverse direction (dashed blue). The ν_e and $\bar{\nu}_e$ fluxes each exhibit a strong dipolar asymmetry, (anti-)aligned with the lepton-number flux dipole, whereas the ν_x flux is nearly isotropic except for a small enhancement in the hemisphere of smallest lepton-number flux (red line).

tios of energy-loss rates to number-loss rates.

This figure reveals the usual behavior during the postbounce accretion phase (compare, e.g., with results by Marek & Janka 2009; Marek, Janka, & Müller 2009; Janka et al. 2012). $\dot{E}_{\nu_e}$ after the shock-breakout burst is very close to $\dot{E}_{\bar{\nu}_e}$ or even slightly larger, while $\langle\epsilon_{\bar{\nu}_e}\rangle$ exceeds $\langle\epsilon_{\nu_e}\rangle$ by a few MeV. Heavy-lepton neutrinos have significantly lower individual luminosities because their production in the accretion layer of the PNS is less efficient due to the lack of charged-current processes, and $\langle\epsilon_{\nu_x}\rangle$ is only slightly larger than $\langle\epsilon_{\bar{\nu}_e}\rangle$ because energy transfers in neutrino-nucleon scatterings reduce the high-energy spectrum of ν_x diffusing outward from their deeper production layers (Raffelt 2001; Keil, Raffelt, & Janka 2003).

Here as well as in the following discussion we mostly focus on the 11.2 $M_\odot$ star. This has two reasons. On the one hand, the 11.2 $M_\odot$ model does not possess the violent SASI episodes which massively affect the neutrino-emission properties in the 20 and 27 $M_\odot$ cases (Tamborra et al. 2013, 2014; Hanke et al. 2013), where they lead to time-dependent variations of the neutrino transport and radiation, superimposed on the hemispheric asymmetry of the lepton-number emission dipole (Fig. 3). Such short-time fluctuations can hamper the easy visibility of the LESA-specific features. On the other hand, outside of the SASI episodes diagnostic quantities that we evaluate for the lepton-emission dipole in the 20 and 27 $M_\odot$ models look, qualitatively and quantitatively, very similar to those that we present in more detail for the 11.2 $M_\odot$ case. This will be shown in Fig. 12.

3.3. *Other flux asymmetries*

The LESA phenomenon is a conspicuous order-unity effect of the directional lepton-number flux variation, but also shows up in other quantities, notably in the directional variation of the individual ν_e and $\bar{\nu}_e$ fluxes. To illustrate this point we show in Fig. 5 these number fluxes as they would be seen by a distant observer relative to their directional averages. We use three viewing directions oriented relative to the lepton-number dipole axis, i.e., an observer located in the direction of maximal lepton-number flux (black lines), the opposite direction of minimal lepton-number flux (red lines), and a typical direction transverse to the dipole axis (dashed blue lines).

A distant observer measures the integrated intensity over a hemisphere of the radiating NS surface, projected on the viewing direction. The corresponding "averaging" over the visible hemisphere eliminates small-scale variations. To evaluate the observational quantities we follow the procedure described in Sect. 3.1 of Müller, Janka, & Wongwathanarat (2012) and in Appendix A of Tamborra et al. (2014) and calculate the observable flux, here the number-flux N, from the ray-by-ray-computed number-flux densities, $F_{\rm n}(\boldsymbol{R})$, at points $\boldsymbol{R}$ on the radiating surface by an integration over the visible hemisphere, cf. Eq. (7) in Müller, Janka, & Wongwathanarat

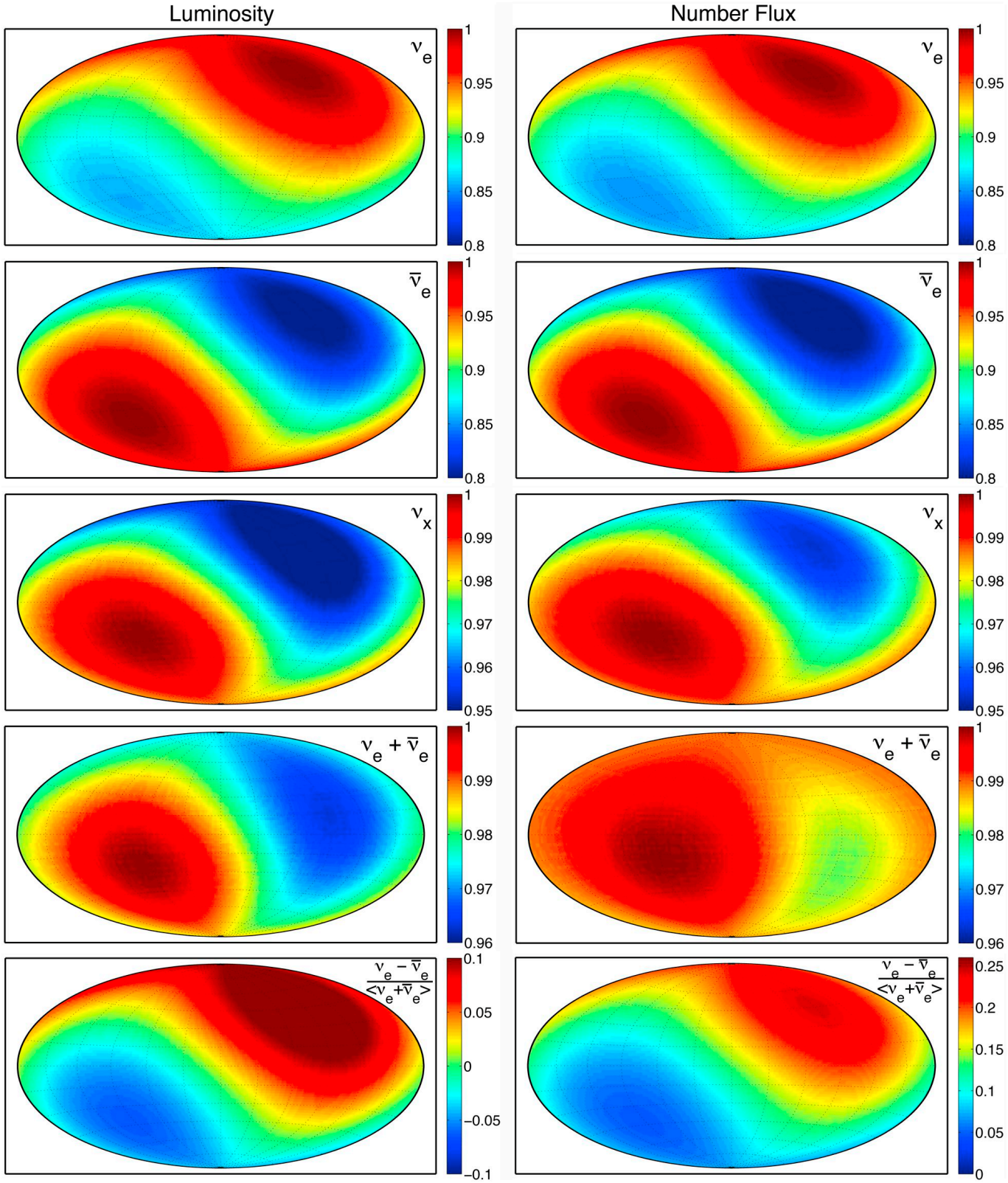

Figure 6. Energy luminosity, L (*left*), and number flux, N (*right*), for the 11.2 $M_\odot$ simulation as functions of viewing direction for a distant observer. The latitudes and longitudes indicated by dotted lines follow the angular coordinate directions of the computational grid. The quantities are hemispheric averages (including projection effects as described in the text) and time integrated over 150–250 ms post bounce. The first three rows show the ν_e, $\bar{\nu}_e$, and heavy-lepton neutrino (ν_x) fluxes, while the fourth row shows $L_{\nu_e} + L_{\bar{\nu}_e}$ and $N_{\nu_e} + N_{\bar{\nu}_e}$. The plotted quantities are normalized to their maximum. In each row the color scale of both images is the same, but the ranges are different in different rows. The bottom row shows the relative excess of ν_e over $\bar{\nu}_e$ emission, i.e., $(L_{\nu_e} - L_{\bar{\nu}_e})/\langle L_{\nu_e} + L_{\bar{\nu}_e} \rangle$ (left) and $(N_{\nu_e} - N_{\bar{\nu}_e})/\langle N_{\nu_e} + N_{\bar{\nu}_e} \rangle$ (right). The denominators are averages over all observer directions. In one hemisphere, the lepton number-emission (ν_e minus $\bar{\nu}_e$) is significantly smaller than the average, while in this hemisphere the energy luminosity of $\bar{\nu}_e$ exceeds that of ν_e. In contrast, the number and energy fluxes of ν_e plus $\bar{\nu}_e$ as well as those of ν_x deviate from isotropy only on the few-percent level.

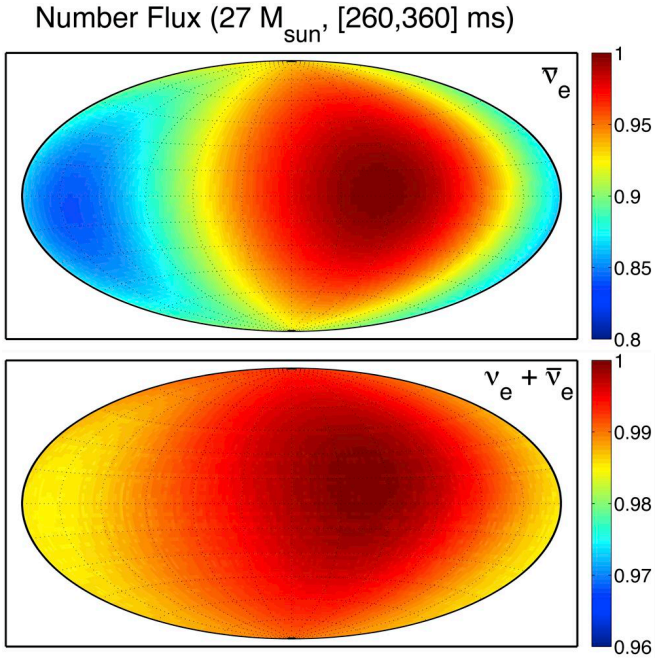

Figure 7. Sky-maps for the 27 $M_\odot$ model analogous to second and fourth panels in the right column of Fig. 6. The time interval of integration, 260–360 ms p.b., is between two episodes of strong SASI activity. The behavior of the heavier-mass models is qualitatively similar to the 11.2 $M_\odot$ case but the spatial orientation of the lepton-emission dipole is different in each case.

(2012):

$$N(t) = 2 \int_{\text{vis.hem.}} \mathrm{d}A \, \cos\vartheta \, F_{\mathrm{n}}(\boldsymbol{R}, t) \left(1 + \frac{3}{2}\cos\vartheta\right). \quad (2)$$

Here ϑ is the zenith angle at point $\boldsymbol{R}$ on the radiating sphere, i.e., the angle between the normal vector of the surface element dA and the observer direction. An analogous relation pertains to the energy luminosity, L, as a function of the energy-flux densities, $F_{\mathrm{e}}(\boldsymbol{R})$,

$$L(t) = 2 \int_{\text{vis.hem.}} \mathrm{d}A \, \cos\vartheta \, F_{\mathrm{e}}(\boldsymbol{R}, t) \left(1 + \frac{3}{2}\cos\vartheta\right), \quad (3)$$

cf. Eq. (5) in Müller, Janka, & Wongwathanarat (2012). The integrands of Eqs. (2) and (3) account for projection effects of the radiating surface elements and limb darkening. In the free-streaming limit, the flux density $F(\boldsymbol{R})$ declines like R^{-2} with distance $R = |\boldsymbol{R}|$ from the source center, while the surface element $\mathrm{d}A = R^2 \mathrm{d}\Omega$ (dΩ being the solid angle) increases with R^2. Therefore, the product $\mathrm{d}A\, F(\boldsymbol{R})$ becomes constant and the integral value is independent of the chosen surface of integration.

Figure 5 shows that in the early phase of postshock convection the directional emission asymmetry remains small. At about 150 ms, however, a stable dipolar pattern emerges and reaches maximum amplitudes of around 10% for ν_e and 15% for $\bar{\nu}_e$ at roughly 180 ms after bounce. A positive amplitude for ν_e is correlated with a negative one for $\bar{\nu}_e$ and vice versa, and local maxima (minima) of the ν_e emission generally coincide in time with minima (maxima) of the $\bar{\nu}_e$ emission. After $t \sim 180$ ms a slow, overall trend of decay of the dipolar emission asymmetry begins, in agreement with our earlier finding in the lepton-number flux, although the relative strength of the lepton-number asymmetry remains large. Note also that we show here the evolution as observed from a fixed direction so that overall trends of the fluxes can be partly caused by a slight drift of the dipole direction.

The dipole asymmetry is large in the ν_e and $\bar{\nu}_e$ fluxes, whereas heavy-lepton neutrinos, ν_x, exhibit at most a few-percent effect. The ν_x emission is slightly enhanced in the direction of small lepton-number (high $\bar{\nu}_e$) flux.

Figure 6 provides similar information for the 11.2 $M_\odot$ model in the form of sky maps for all viewing directions of a distant observer. The temporal stability of the dipole pattern justifies time averaging instead of individual snapshots. In particular, we average over 150–250 ms p.b., when the dipole effect is particularly strong. The left column provides the luminosities, L, for ν_e, $\bar{\nu}_e$, ν_x, as well as ν_e plus $\bar{\nu}_e$, and ν_e minus $\bar{\nu}_e$, all normalized to their directional maxima except for the difference plot, which is normalized to the all-sky average of $L_{\nu_e} + L_{\bar{\nu}_e}$. The right column shows analogous information for the corresponding number fluxes, N.

Both luminosities and number fluxes clearly show the emission dipole (anti-)aligned with the lepton-number dipole axis. While the maximum variation amplitudes of ν_e and $\bar{\nu}_e$ fluxes are approximately ±10% in the two dipole directions, heavy-lepton neutrinos show just about ±2% variations. In contrast to the individual luminosities and number fluxes, the sums $L_{\nu_e} + L_{\bar{\nu}_e}$ and $N_{\nu_e} + N_{\bar{\nu}_e}$, vary only on the few-percent level. We also note that the relative variation of the energy-flux difference, $L_{\nu_e} - L_{\bar{\nu}_e}$, is a bit smaller than the hemispheric variation of the number-flux difference $N_{\nu_e} - N_{\bar{\nu}_e}$. Most importantly, while the former can be positive or negative, the latter is positive in all directions. This shift of the asymmetry variation in the luminosity difference corresponds to considerably larger $\bar{\nu}_e$ energies relative to ν_e.

In contrast, the 27 $M_\odot$ run with its episodes of strong SASI shock sloshing and spiralling motions (see Hanke et al. 2013) exhibits large-amplitude, quasiperiodic neutrino emission modulations with dipolar asymmetry in all flavors (Tamborra et al. 2013, 2014). In addition, however, the 27 $M_\odot$ model also shows a steady lepton-number emission dipole, i.e., a long-lasting and non-oscillating dipole in the lepton-number flux (ν_e minus $\bar{\nu}_e$). We present a sky-map of the $\bar{\nu}_e$ number flux as well as the total ν_e plus $\bar{\nu}_e$ flux in Fig. 7. To avoid any confusion with SASI activity, we show a time-averaged signal here as seen by a distant observer taken between the two episodes of SASI activity, i.e., integrated over the p.b. interval of 260–360 ms. In qualitative agreement with the 11.2 $M_\odot$ case, there is a clear dipole feature in the $\bar{\nu}_e$ flux, whereas in the sum flux the dipole variation is weak—the individual ν_e and $\bar{\nu}_e$ fluxes are again anti-correlated.

The LESA dipole directions of our three stellar models do not show any correlation with each other (cf. Fig. 3), and they are uncorrelated with the numerical grid. Moreover, the LESA dipole direction has no clear correlation with the main direction of SASI sloshing or with the plane of SASI spiralling motions. Figure 8 displays the evolution of the SASI and LESA directions during the first SASI-dominated phases of the 20 $M_\odot$ and 27 $M_\odot$ models (170–300 ms and 170–260 ms, respectively). In the former case, the LESA dipole direction is clearly far outside of the plane defined by the movements of the SASI shock-deformation vector (implying that the LESA dipole vector and the normal vector of the SASI plane are nearly aligned), while in the latter case the LESA dipole happens to be close to the SASI plane. This suggests that the relative orientations of SASI and of the lepton-number emission dipole are chosen randomly and that both effects are independent phenomena. Nevertheless, both seem to be able

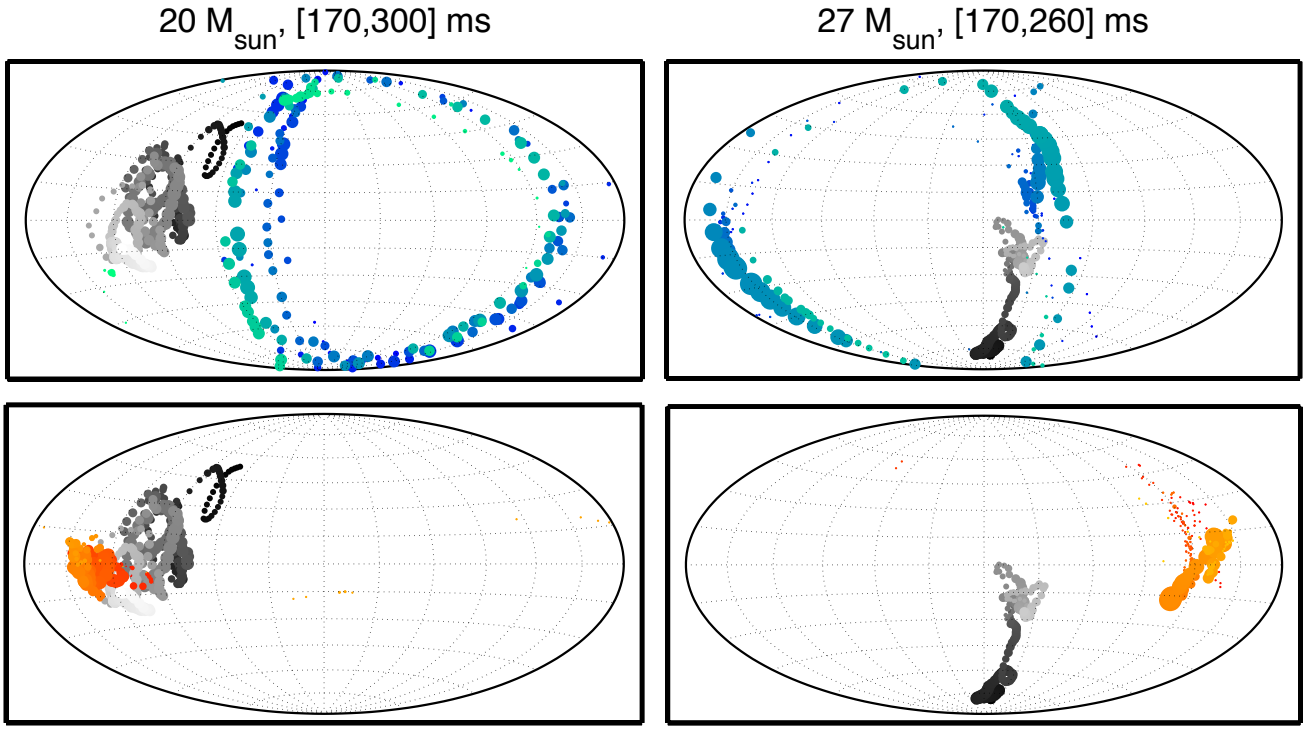

Figure 8. Evolution of LESA and SASI directions during the first SASI-dominated episodes of the 20 $M_\odot$ model (*left*) and 27 $M_\odot$ model (*right*). The corresponding time intervals are given above the columns. Black and gray dots mark the path of the positive LESA dipole direction (associated with maximal excess of the ν_e emission). Colored dots show the path of the SASI shock-deformation vector, which describes the plane of the SASI spiral motion (*upper panels*), and the path of the instantaneous normal vector, which represents the direction orthogonal to the SASI plane (*bottom panels*). The size of the dots scales with the vector lengths and thus increases with the LESA and SASI amplitudes, and the color hues become lighter as time progresses. While the LESA dipole lies close to the SASI plane in the 27 $M_\odot$ model, both are nearly perpendicular to each other in the 20 $M_\odot$ case.

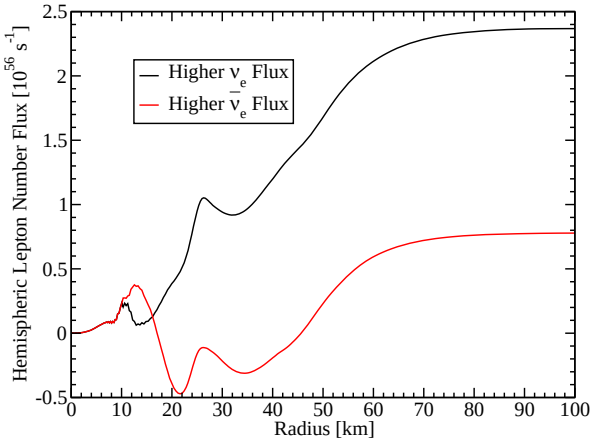

Figure 9. Radial evolution of the lepton-number emission in the hemisphere where the lepton flux is maximal (black) and minimal (red) for the 11.2 $M_\odot$ simulation at 210 ms p.b. The fluxes are integrated over the hemispheres without projection effects so that their sum is the total lepton-number flux traversing a spherical surface of given radius. The lepton-number flux asymmetry originates mostly from deep inside the PNS, i.e., from the hot PNS mantle below the neutrinosphere that is located at approximately 35 km, whereas a more spherically symmetric component of the lepton-number flux develops in the surrounding, semi-transparent cooling layer and is fed by the accretion of lepton-rich material.

to influence each other as we will discuss later (Sect. 4.4).

3.4. *Radial evolution of the emission dipole*

We next investigate the spatial origin of the lepton-number flux asymmetry. To this end we consider the evolutionary stage at 210 ms p.b. of the 11.2 $M_\odot$ model when the lepton-number dipole has reached a large value. Figure 9 shows the radial evolution of the lepton-number (ν_e minus $\bar{\nu}_e$) flux for the two hemispheres where it is maximal and minimal, respectively. The integration avoids any projection or observer effects—the sum of the two hemispheric values yields the total lepton-number flux traversing a spherical shell of given radius. It is intriguing that most of the hemispheric difference builds up in the PNS mantle layer *below* the (average) neutrinosphere, which is located here at around 35 km. At this radius, the lepton-flux difference has nearly reached its asymptotic value, whereas only about 20–25% (or 3–4 $\times$ 10^{55} s^{-1}) arise at larger radii and are therefore more directly associated with the hemispheric asymmetry of the accretion flow (cf. Sect. 4.1).

A different way of visualizing the radial evolution of the lepton-number flux is to study it along individual radial "rays" of our transport scheme. To this end we have performed a cut of our 11.2 $M_\odot$ model in a plane containing the dipole direction at 210 ms p.b. Figure 10 shows the result with a color coding corresponding to the radial lepton-number flux as a function of location in this cut plane. The downward direction in the plots is the direction of maximum lepton-number flux. It is apparent that this hemisphere shows stronger convection inside the PNS than the other hemisphere. The flux asymmetry arises far below the average neutrinosphere, here indicated by a white circle.

Most of the overall lepton-number emission (the monopole of the emission distribution) builds up in the envelope (i.e., the neutrino-cooling) region above the NS and is fed by the accretion downflows of lepton-rich material, whereas most of

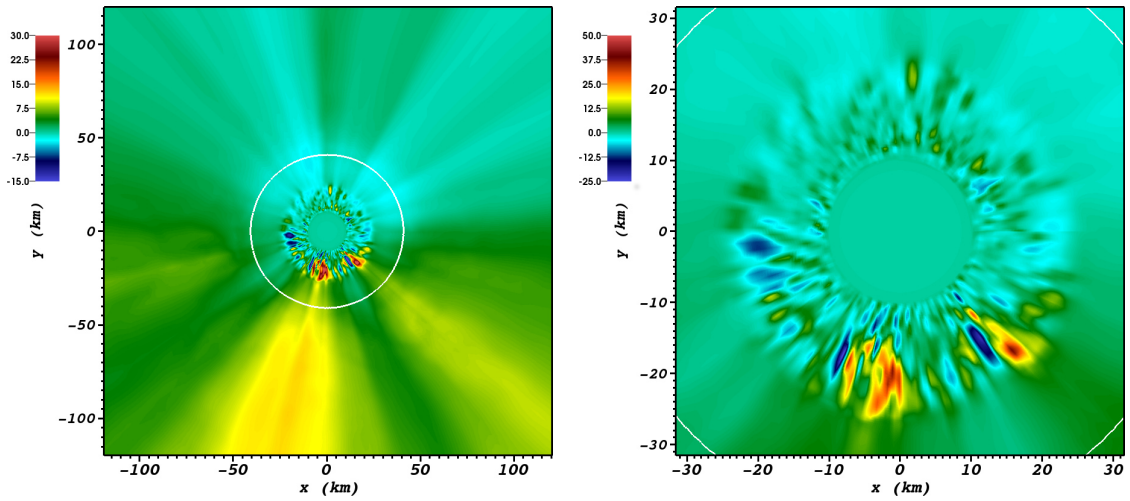

Figure 10. Radial evolution of the lepton-number flux in the 11.2 $M_\odot$ model at 210 ms p.b. (same moment as in Fig. 9). Shown is the color-coded isotropic equivalent of the lepton number flux, i.e., $4\pi r^2 (F_{\nu_e} - F_{\bar{\nu}_e})$ in 10^{56} s^{-1}, along angular "rays" of the transport simulation. The cut plane includes the direction of maximal lepton emission (bottom of panels) and the opposite direction of minimal lepton emission (top of cut). The average neutrinosphere is at about 35 km (white circle). The right panel is a zoom of the left one. PNS convection is clearly visible, with stronger activity in the hemisphere of maximal lepton-number flux (bottom direction).

the dipole builds up around the PNS convection zone deep inside the NS and below the neutrinosphere. While the accretion flow also shows a dipole asymmetry as we will see, it is not responsible for the main effect of the asymmetry of the lepton-number emission.

3.5. *Asymmetry of electron density distribution*

Most of the lepton number stored in the PNS and its accretion layer is in the form of electrons, whereas it is emitted in the form of a ν_e-$\bar{\nu}_e$ number-flux difference. Therefore, it is instructive to inspect the electron density distribution in those regions of the PNS where the lepton-flux dipolar asymmetry originates. Figure 11 shows color-coded Y_e distributions of the 11.2 $M_\odot$ model in cut planes containing the dipole axis in analogy to Fig. 10 and with the same orientation, i.e., bottom is the hemisphere of largest lepton-number emission. We also show iso-density contours as white circles—the density stratification is perfectly spherical and concentric around the center of mass (which essentially coincides with the coordinate origin) because of the extreme strength of the gravity field of the PNS. The outermost contour, corresponding to 3×10^{11} g cm^{-3}, is somewhat interior to the average neutrinosphere.

The four different postbounce moments correspond to the ones shown in Fig. 1 and span the time when the lepton-emission dipole begins to form (148 ms p.b.) all the way to a time when it is fully developed, but still before any noticeable decay takes place (240 ms). We see the development of a more electron-depleted region in the upper hemisphere, where a smaller lepton-number flux originates, while the bottom hemisphere, where a larger lepton-number flux originates, exhibits more electron-rich material. The growth of the hemispheric asymmetry of the lepton distribution in the PNS mantle region below the neutrinosphere is clearly visible as the compact remnant deleptonizes and contracts between $t \sim 150$ ms (top left) and $t = 210$ ms (bottom left). At around this later time the most extreme hemispheric difference is reached with an electron fraction difference of up to $\Delta Y_e \sim 0.03$–0.06 on some density levels. As time and lepton emission progress, the hemispheric differences tend to decrease (bottom right).

The asymmetry of the Y_e distribution not only explains the emission dipoles of ν_e and $\bar{\nu}_e$, it also explains why the number flux of heavy-lepton neutrinos, ν_x, is somewhat amplified (on the percent level) in the direction of the smaller lepton-number flux, which is the direction of stronger $\bar{\nu}_e$ emission (cf. Figs. 5 and 6). Because the annihilation of e^+e^- and $\nu_e\bar{\nu}_e$ pairs yields important contributions to the ν_x number flux, in particular at lower densities (whereas at high densities the production by nucleon-nucleon bremsstrahlung dominates; see Raffelt 2001; Buras et al. 2003; Keil, Raffelt, & Janka 2003 for details), the larger positron and $\bar{\nu}_e$ abundances on this side of the PNS also foster the emission of heavy-lepton neutrinos.

4. DRIVING MECHANISM OF LESA

4.1. *Asymmetry of mass-accretion flow*

The lepton-flux asymmetry originates deep inside the PNS, below the neutrinosphere, and several phenomenological observations form a consistent picture, e.g., the lepton-emission asymmetry, the PNS convection asymmetry, the asymmetric Y_e distribution, and the small ν_x emission asymmetry. However, these manifestations do not yet provide a hydrodynamical explanation of how these effects first arise and then stabilize themselves in a long-lasting, only slowly evolving pattern. Moreover, the initial growth of the dipole distribution over 100–150 ms is parallel to the growth of convective overturn in the gain region below the stalled shock wave.

The most plausible physical connection between the asymmetries deep in the PNS and hydrodynamical properties of the envelope derives from asymmetric mass-accretion flows. To study this hypothesis we consider the time evolution of the mass accretion flow in our usual two hemispheres defined by maximal and minimal lepton-number emission, shown in Fig. 12 for all three considered progenitors (top row). At a time when the dipole begins to form in earnest, we notice a significant hemispheric asymmetry of the mass accretion rate such that the hemisphere of larger lepton-number flux also has the systematically larger mass accretion rate.

This flow fluctuates strongly because of convective perturbations and (in the 20 and 27 $M_\odot$ models) SASI mass motions,

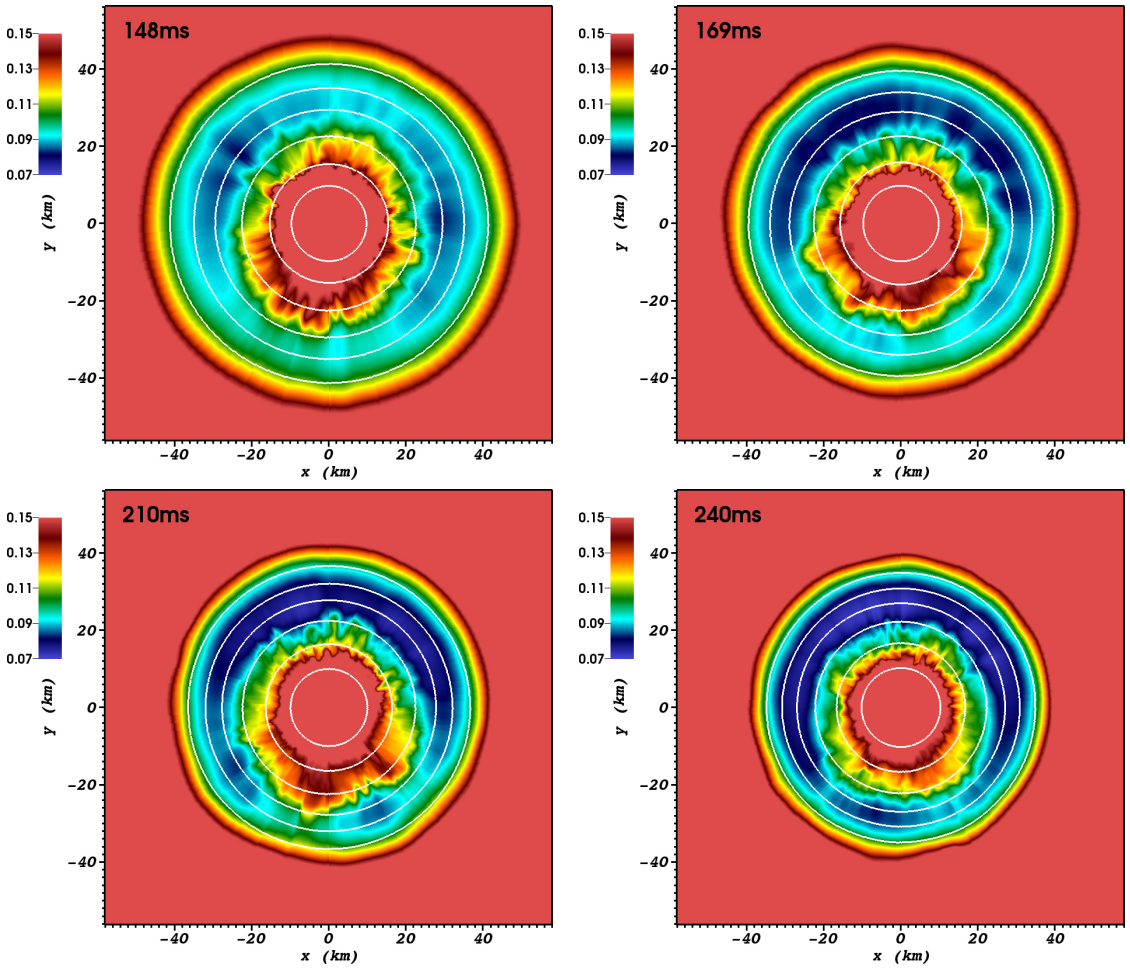

Figure 11. Distribution of the electron fraction, Y_e, in the PNS and its immediate surroundings for the 11.2 $M_\odot$ model at the indicated p.b. times. The cut plane is the same as in Fig. 10, i.e., it contains the dipole axis with the direction of maximal lepton-number emission being downward in these panels. The color scale saturates when $Y_e > 0.15$ and was chosen to highlight the Y_e variations in the PNS mantle region around the central, lepton-rich core and below the neutrinosphere (which roughly coincides with the outermost white circle). The white circles are isodensity contours at the levels of $3{\times}10^{11}$, 10^{12}, $3{\times}10^{12}$, 10^{13}, $3{\times}10^{13}$, and 10^{14} g cm^{-3}. Notice the development of a more strongly deleptonized shell in the upper hemisphere (direction of minimal lepton-number flux), while in the bottom hemisphere the lepton-number fraction is larger. In this hemisphere, the mass accretion rate is larger, supplying a larger amount of fresh lepton number.

but on average exhibits a time-dependent anisotropy of 30–50% for the 11.2 $M_\odot$ case and of 10–25% for the other two progenitors. On average it carries considerably more fresh lepton number to the central compact object on one side than on the other. The lepton-rich flow partially deleptonizes by neutrino emission before it spreads out below the PNS surface to settle into the PNS mantle[4], but it is still more lepton-rich than the deleptonized material that is already present in this region. Because it is specifically lighter (containing a higher number fraction of electrons and protons instead of heavier neutrons), the lepton-rich gas does not efficiently mix with the deleptonized plasma. Instead, it accumulates on one side of the PNS and pushes the more deleptonized fluid out of the way, towards the opposite hemisphere.

The full explanation for the Y_e distribution is actually even more complex. The accretion inflow of lepton number cannot explain the entire Y_e asymmetry in the PNS mantle. On the one hand, the accretion downflows deleptonize nearly identically during their infall from different directions, fairly independently of the local mass-flux density in the convective downdrafts that carry the accretion flow towards the PNS. Some of the greenish areas in the lower hemisphere of Fig. 11, which have no counterpart on the upper side, have possibly inherited their electons from accretion flows. However, the red, orange and yellow bulges, which reach outward from the dense, high-Y_e core most prominently in the lower hemisphere, cannot come from the same origin. They are located in the convective shell of the PNS, which is interior to the neutrinospheres, and they thus suggest an enhanced efficiency of the convective lepton-number transport out from the inner core. The convective region inside of the PNS can be recognized as a circular ring of short-wavelength color variations between ∼12 km and ∼25 km in the right panel of Fig. 10. This region is more pronounced in the lower hemisphere, indicating stronger PNS convection effects in this direction, by which lepton number is pulled up from the central, lepton-rich high-density core. This dredge-up explains the presence of high-Y_e patches (red, orange, and yellow in Fig. 11) extending outward from the inner core region.

[4] Consistent with our discussion of the radial evolution of the lepton-emission dipole in Sect. 3.4 that was based on Fig. 9, we now independently confirm that the lepton-number loss ($\Delta Y_e \approx 0.4$) associated with the accretion-rate difference between the two hemispheres, $\Delta\dot{M} \lesssim 0.08\,M_\odot\,\mathrm{s}^{-1}$ for the 11.2 $M_\odot$ model (Fig. 12, left column), accounts for a lepton-number flux of at most $4{\times}10^{55}\,\mathrm{s}^{-1}$ and therefore can explain at most 25% of the lepton-emission dipole.

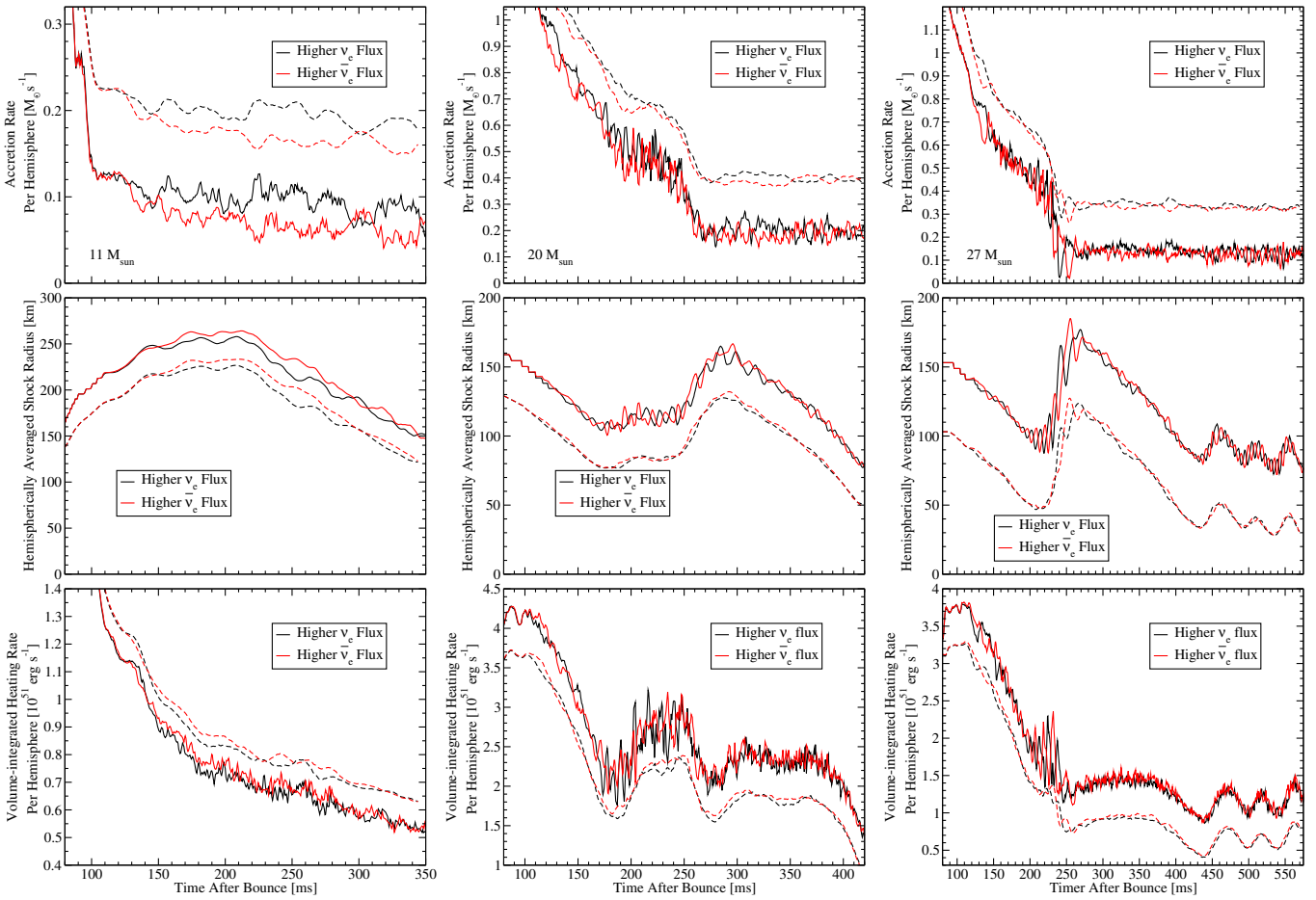

Figure 12. Time evolution of quantities in the postshock accretion layer of the 11.2 $M_\odot$ (*left column*), 20 $M_\odot$ (*middle column*), and 27 $M_\odot$ (*right column*) models for the hemisphere of large lepton-number flux, i.e., large ν_e flux (black lines), and the opposite hemisphere of larger $\bar{\nu}_e$ flux (red lines). The dashed lines show running averages over 10 ms intervals, shifted vertically for better visibility. The two hemispheres of the analysis follow the slowly drifting LESA dipole direction. *Top:* Mass accretion rate, measured half way between the average radius of the stalled SN shock and the average gain radius. *Middle:* Average shock radius. *Bottom:* Volume-integrated neutrino-heating rate in the gain layer. The plots visualize important components of the crucial feedback loop consisting of asymmetric accretion rate, asymmetric lepton-number flux, asymmetric neutrino heating rate, and dipole deformation of the shock front as explained in the main text and Fig. 15. In all models the mass accretion rate is systematically and persistently higher in the hemisphere with larger ν_e flux (black lines), whereas the shock radius and heating rate are greater in the opposite hemisphere. In the 20 and 27 $M_\odot$ models with episodes of prominent SASI activity (marked in Fig. 3) the effect is most clearly visible outside of the SASI phases, when convective overturn is the dominant hydrodynamic instability in the neutrino-heated postshock layer.

Convective activity inside the PNS is constrained to a shell that surrounds the convectively stable core. The size of the convection cells is roughly defined by the radial scale of the active layer. Therefore, a volume-filling convective dipole mode is absent and the formation of a low-mode dipolar asymmetry of the lepton transport is puzzling. This argument supports a driving mechanism connected to the global accretion asymmetry. It seems that convective transport of lepton (electron) number in the deeper PNS mantle region might be amplified when accretion downflows impinge into the PNS, presumably because shear flows, turbulence, and gravity waves, which are instigated in the outer layers of the PNS mantle as a consequence of such violent impacts, can act in a destabilizing way on convectively nearly neutral or marginally stable statifications. Also the contraction of the PNS might play an important role during the growth phase of the dipole mode. Postshock overturn develops in parallel to a phase of strong PNS contraction. Since the NS mantle layer settles to increasing densities, convection cannot reach a steady state in which perturbations connected to the impact of accretion downflows may be washed out on the typical timescales of small-scale lepton transport. Instead, hemispheric asymmetries imprinted at early times, when matter still resides at low densities with short restoring timescales, may be carried to higher densities and thus may get frozen in for much longer periods, becoming the initial seeds for a subsequent growth towards the global dipolar asymmetry. A more detailed analysis of the dynamical interaction of accretion stream impacts in the outer layers of the PNS and convection in the contracting PNS mantle is deferred to future work.

The low-mode dipolar asymmetry of the lepton-number distribution in the PNS is therefore a consequence of the strong gravity, which on the one hand tends to spread out flows and to smoothen structures along equipotential surfaces and on the other hand defines an environment where buoyancy effects play an extremely important role.

4.2. *Asymmetry of gain-layer convection and shock-wave radius*

One may wonder if the asymmetric accretion flow has a visible correspondence in the structure of the large-scale convection in the gain region. To investigate this question we show in

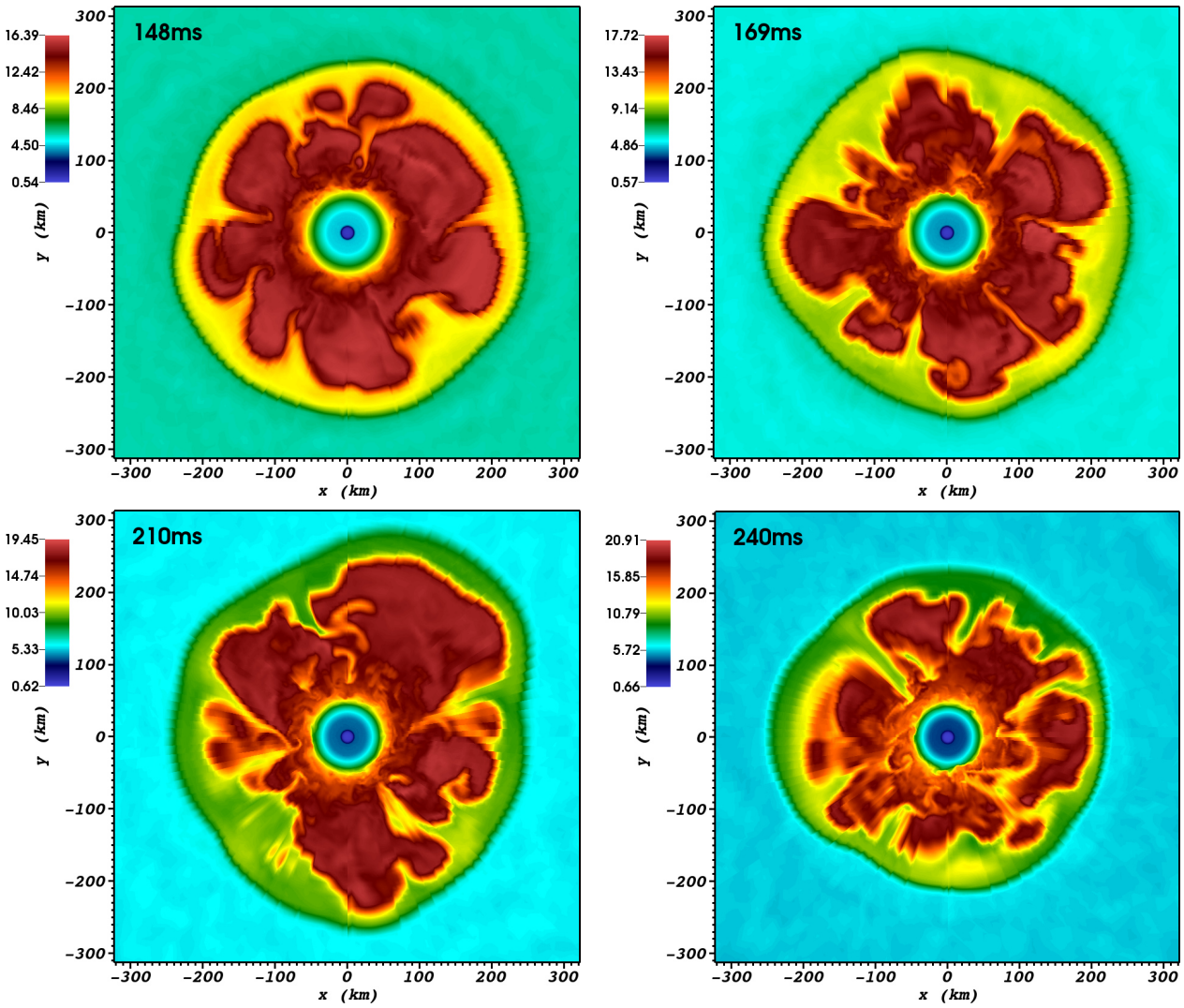

Figure 13. Entropy distribution in the postshock region of the 11.2 $M_\odot$ simulation at the indicated p.b. times. The cut plane is the same as in Figs. 10 and 11, i.e., it contains the dipole direction, where downward is the direction of maximum lepton-number flux. While a global asymmetry between the upper and lower hemispheres is hardly visible during the early stages when the lepton emission anisotropy just begins to develop (see Fig. 5), stronger convection in the upper hemisphere during the later stages (*bottom panels*) can be inferred from the larger buoyant bubbles and larger average shock radius on this side.

Fig. 13 entropy distributions of the 11.2 $M_\odot$ model in the same cut planes that were used in Fig. 11 for the Y_e distribution, i.e., the plane contains the dipole direction and downward is the direction of maximum lepton-number flux. In contrast to the clear hemispheric differences of the mass accretion rate in the postshock layer (Fig. 12, top left panel), associated differences in the region of convective overturn are not clearly visible in the entropy cuts or in the earlier visualizations of Fig. 2. A closer inspection of the entropy cuts (Fig. 13) reveals that in the lower two panels (t = 210 and 240 ms p.b.) the convective plumes are bigger and push the shock to a slightly larger radius in the upper hemisphere. Moreover, the convective downdrafts that carry the accretion flow to the PNS are more numerous (lower left panel) and the flow close to the PNS is more vigorous (lower right panel) on the opposite side. Because the convective mass motions are highly turbulent and time variable, however, one should be cautious with conclusions based on selected snapshots.

To be more quantitative, the average shock radii in both hemispheres are shown in the middle panel (left column) of Fig. 12. Indeed, from ∼150 ms onwards a clear and persistent difference, aside from fluctuations, of 10–20 km (6–7% of the average shock radius) is found.

The one-sided increase of the average shock-wave radius is actually the physical cause for the accretion-flow asymmetry, because the spherical infall from larger radial distances is deflected and channelled preferentially toward the hemisphere of smaller shock-wave radius. One should notice the anti-correlation between mass-accretion flow and shock-wave radius in Fig. 12—the hemisphere of increased accretion flow (black line) is the hemisphere of reduced shock-wave radius. It is important in this context to remember that the preshock accretion flow is spherically symmetric except for imposed, small-scale random perturbations.

4.3. *Asymmetry of neutrino-heating rates*

But how can this dipolar shock deformation be maintained in a persistent and long-lasting manner despite vigorous convection behind the shock? Here an interesting, self-sustaining feedback mechanism comes into play, in which the lepton-emission dipole asymmetry itself facilitates, supports, and stabilizes the conditions for its existence. The key point is

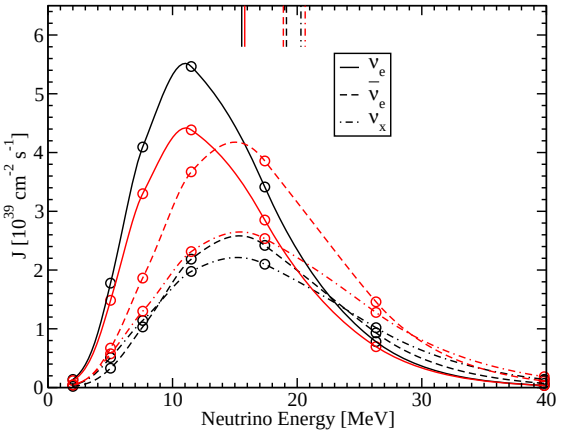

Figure 14. Energy spectra of ν_e, $\bar{\nu}_e$, and ν_x for the 11.2 $M_\odot$ model at 210 ms p.b. (same time as in Fig. 9). The spectra are for rays in the direction of maximal (black) and minimal (red) lepton-number flux, evaluated at a distance of 400 km in the comoving frame of the accretion flow, which is spherically symmetric at this radius. We provide the monochromatic energy moment $J = \Delta E\, c/(4\pi\, \Delta\epsilon_\nu)$ with ΔE being the energy density in neutrino energy bin $\Delta\epsilon_\nu$. The tick marks at the upper edge of the plot mark the rms energies. The neutrino spectral shape is very similar in these opposite directions for each species, whereas the differences in overall normalization reflect the dipolar flux asymmetries.

that the lepton-flux asymmetry implies a neutrino-heating rate asymmetry in the gain region below the shock. In particular, the heating rate is larger in the hemisphere of smaller lepton-number flux (red lines in Fig. 12), which is the hemisphere of more vigorous gain-region convection and increased shock-wave radius. In the bottom panels of Fig. 12 we show volume-integrated heating rates in the gain layers of both hemispheres as functions of time, and indeed there is a systematic offset between the two hemispheres. Stronger neutrino heating leads to more powerful convective buoyancy and this naturally pushes the radius of the stalled shock farther out in one hemisphere compared to the opposite hemisphere, where the neutrino-energy deposition is weaker. So in the hemisphere of small lepton-number flux we have an increased heating rate, increased shock-wave radius, reduced mass-accretion flow, and therefore reduced lepton-number flux.

In order to further discuss the heating asymmetry we now consider the characteristic spectral properties of the radiated neutrinos for our 11.2 $M_\odot$ model. The $\bar{\nu}_e$ are emitted by the PNS with significantly higher average energies than ν_e. Typically, $\langle\epsilon_{\bar{\nu}_e}\rangle$ exceeds $\langle\epsilon_{\nu_e}\rangle$ by 3–3.5 MeV, averaged over all emission directions as illustrated by Fig. 4. These spectral differences also exist separately in both hemispheres, and they manifest themselves also in the rms energies as shown in Fig. 14, where we display the emitted energy spectra for our previous 210 ms snapshot of the 11.2 $M_\odot$ model. Comparing the radiated energy spectra of ν_e, $\bar{\nu}_e$, and ν_x on two selected radial rays close to the directions of maximal (black) and minimal lepton-number flux (red), the spectra differ primarily in the normalizations, whereas the spectral shapes are very similar (Fig. 14). Correspondingly, the rms energies, indicated by tick marks at the upper edge of the plot, are 15.6, 19.1 and 20.3 MeV for ν_e, $\bar{\nu}_e$ and ν_x, respectively, in the direction of maximum lepton-number flux, and very similar values of 15.8, 18.9 and 20.6 MeV are found in the opposite direction. The normalized moments of the energy spectra for each neutrino type are nearly identical in both hemispheres.

The increased heating rate in the hemisphere of small lepton-number flux (more similar ν_e and $\bar{\nu}_e$ number fluxes) can now be understood as follows. For the dominant processes of ν_e absorption on free neutrons and $\bar{\nu}_e$ absorption on free protons the heating rate per nucleon can be approximated by (cf. Janka 2001)

$$\dot{q} \propto \frac{\sigma_0}{r^2}\left(L_{\nu_e}\left\langle\epsilon^2_{\nu_e}\right\rangle Y_n + L_{\bar{\nu}_e}\left\langle\epsilon^2_{\bar{\nu}_e}\right\rangle Y_p\right), \qquad (4)$$

where σ_0 is the normalizing cross section, r^{-2} describes the radial flux dilution far away from the neutrinosphere, Y_n and Y_p are the number fractions of free neutrons and protons, respectively, L_ν stands for the neutrino luminosities, and $\langle\epsilon^2_\nu\rangle$ denotes the squared rms energy of the energy flux. Since $\bar{\nu}_e$ are radiated with higher rms energies, the neutrino heating will be stronger in the hemisphere where the $\bar{\nu}_e$ number emission is relatively enhanced, despite the nearly isotropic luminosity sum of ν_e plus $\bar{\nu}_e$. The effect is amplified by the fact that in this hemisphere, the $\bar{\nu}_e$ energy flux even exceeds that of ν_e (cf. Fig. 6, lower left panel).

Quantitatively, the numerical difference between the heating rates in the two hemispheres seen in Fig. 12 (bottom left panel) is roughly 5%. This finding can easily be verified by estimating the ratio of the heating rates between the directions of low and high lepton-number flux, $\dot{q}_{\rm low}/\dot{q}_{\rm high}$. Using Eq. (4), assuming Y_p and Y_n to vary little with direction, and adopting a ratio of the squared rms energies of $\langle\epsilon^2_{\bar{\nu}_e}\rangle/\langle\epsilon^2_{\nu_e}\rangle \approx 1.46$ in both hemispheres (Fig. 14) as well as amplitudes of 10–15% for the dipolar asymmetry of the ν_e and $\bar{\nu}_e$ energy fluxes (Figs. 5 and 6), we obtain $\dot{q}_{\rm low}/\dot{q}_{\rm high} \sim 1.04$–$1.06$. The numerical results in the bottom panels of Fig. 12 are based on an integration over the volumes of the gain layer in both hemispheres while these hemispheres were moved with the slowly wandering direction of the LESA dipole.

4.4. *Asymmetries in models with SASI activity*

As expected from the fact that the neutrino emission exhibits all the characteristic LESA features also in our 20 and 27 $M_\odot$ models, the hemispheric asymmetries described above mostly for the 11.2 $M_\odot$ case are also found in the other two progenitors (Fig. 12). However, the SASI mass motions in these cases lead to short-timescale neutrino-emission modulations superimposed on the dipolar lepton emission asymmetry (see Tamborra et al. 2014), and the large-amplitude SASI-induced variations of the postshock accretion flow can mask the global, hemispheric differences of the mass accretion rate, shock radius, and neutrino-heating rate associated with the LESA phenomenon during the phases of strong SASI activity.

This problem for the analysis is more conspicuous for the 27 $M_\odot$ simulation (Fig. 12, right column), where the higher mass accretion rate, smaller shock radius and neutrino heating rate in the hemisphere of excess ν_e flux are clearly visible only during the SASI-quiet episodes, i.e. before 170 ms and between 260 ms and 420 ms. In constrast, the familiar hemispheric asymmetries of these quantities can be seen at essentially all times in the 20 $M_\odot$ model, despite the violent SASI in the time interval from 170 ms to 305 ms.

This difference between both models is connected to the different relative orientations of the SASI plane and the LESA dipole vector in these models during the first SASI episodes (cf. Fig. 8). While in the 27 $M_\odot$ model the LESA dipole lies in the plane of the SASI spiralling, it is nearly orthogonal to the SASI plane in the 20 $M_\odot$ case. In the former model the mass-accretion, gain-layer convection, and heating asymmetries de-

scribed in Sects. 4.1–4.3 are therefore strongly perturbed by the violent mass flows associated with the SASI, whereas in the $20\,M_\odot$ model these hemispheric asymmetries seem to be less affected by the SASI flows because they proceed in the direction perpendicular to the SASI plane. It is important to note that usually also during SASI-active phases convective overturn as a consequence of neutrino heating is still present.

Therefore SASI mass motions in the postshock layer interfere with the LESA phenomenon in different ways, depending on the orientation of the LESA direction relative to the plane of SASI sloshing and spiralling. If the lepton-emission dipole happens to coincide with the SASI plane the violent modulations of the postshock accretion flow by the SASI seem to be able to prevent further growth of the LESA dipole (cf. Sect. 3.1) and to enforce a gradual drift of the dipole direction, see the right panels of Figs. 3 and 8 for the first SASI phase (between 170 and 260 ms p.b.) of our $27\,M_\odot$ model. If, in contrast, the LESA vector is incidentally perpendicular to the SASI plane, the growth of the LESA amplitude is not impeded and the LESA direction may describe quasi-periodic wobbling around a mean orientation, see the SASI-active episode of our $20\,M_\odot$ simulation from 170 ms to 305 ms in the middle panels of Fig. 3 and the left panels of Fig. 8. The LESA-SASI interference is therefore complex and any behavior intermediate between these extrema might be possible.

5. OVERALL PICTURE OF THE LESA PHENOMENON

5.1. *Two interlocking cycles*

From our discussion so far a picture of the LESA phenomenon emerges that involves a machinery consisting of two major interacting parts. One consists of asymmetric PNS convection and concomitant asymmetric lepton-number emission. The other consists of asymmetric mass-accretion regulated by asymmetric neutrino emission through asymmetric neutrino heating in the gain layer.

We re-capitulate and summarize the cog-wheels of this machinery in the sketch of Fig. 15. It is oriented in the same way as our previous cut-planes, i.e., the lepton-number emission maximum is in the downward direction. In our line plots, black curves correspond to properties in the downward direction or lower hemisphere, red curves to the upward direction (or hemisphere), which is the hemisphere of minimal lepton-number flux emission.

In the inner parts of Fig. 15, the mass center is marked by a black dot, surrounded by concentric red circular regions which show the density stratification inside the newly formed NS. The long-dashed line indicates the location of the neutrinosphere(s). Blue circles represent levels of constant electron fraction (Y_e). The upward displacement of the light-blue region visualizes schematically a dipolar asymmetry of the deleptonization in the NS mantle region enclosed by the neutrinosphere: While in the top hemisphere the layer below the neutrinosphere has deleptonized more strongly due to the preceding and ongoing emission of electron neutrinos (the light-blue region there is bigger), the bottom hemisphere contains a larger fraction of electrons (indicated by the larger red area).

This dipolar asymmetry of the Y_e distribution in the PNS mantle is a consequence of a pronounced hemispheric difference in the mass flow towards the compact object. The latter accretes matter at a significantly higher rate on one side and thus receives a greater inflow of fresh lepton number in this hemisphere (bottom in Fig. 15). Even more important, however, is an indirect effect connected with the mass accretion. As the accretion streams impinge onto the PNS they instigate turbulence and gravity waves, which enhance convection in the deeper mantle layers of the PNS, dredging up electrons from the central, lepton-rich dense core (visualized in Fig. 15 by the larger convective loops in the lower hemisphere). Lepton number carried away by the outgoing neutrino fluxes is therefore replenished by electrons delivered by accretion downdrafts as well as those pulled outward in convective flows that reach deeper into the PNS core. Since the underlying processes are nonisotropic and more efficient in one hemisphere, the deleptonized mantle layer of the PNS exhibits a long-lasting dipolar asymmetry of the Y_e distribution.

The anisotropic accretion flow towards the PNS is indicated by the two red accretion-stream lines. Such an accretion asymmetry in the convectively stirred postshock layer should be understood in a time-averaged sense, emerging effectively from a strongly fluctuating accretion-flow pattern. The convective activity in the region between gain radius (short-dashed line) and shock is symbolized by the up- and down-going loops for the convective overturn motions of rising and sinking gas. The accretion asymmetry is caused by a dipolar shock deformation, which—again in a time-averaged sense—is associated with a larger radius of the accretion shock (thick, black outer ellipsoidal line) in the upper hemisphere. This leads to a deflection of the radial accretion flow when the collapsing matter crosses the shock front, because the tangential velocity component is conserved whereas the perpendicular velocity component is reduced by the flow deceleration according to the shock-jump conditions. The deflection of the postshock flow feeds, on average, the lower PNS hemisphere with a higher mass accretion rate.

In this picture, the dipole asymmetry of the neutrino lepton-number flux is a self-sustained, self-stabilizing phenomenon, because the different spectral properties of ν_e and $\bar{\nu}_e$ ensure more efficient neutrino heating on the side of the lower mass accretion rate and thus lower radiated lepton-number flux. Stronger heating in this hemisphere supports stronger convection and a greater shock radius, thus maintaining the shock deformation that is responsible for the deflection of the accretion flow and the enhanced mass accretion rate reaching the opposite side of the PNS. Neutrinos therefore play a crucial role in this nonradial instability, which leads to a long-lasting, stable asphericity of the postbounce accretion situation.

5.2. *Memory effect in the PNS*

The LESA effect is not "switched off" by the appearance of strong SASI activity, a surprising finding because one might imagine that violent sloshing and spiral modes could interrupt the feedback loop which is the driving cause for LESA. However, LESA has substantial inertia built into its machinery, where the Y_e distribution and related PNS convection asymmetry play the role of a flywheel that keeps going even if the driving engine has been temporarily disabled. Once SASI has subsided, the continuing asymmetric lepton emission from the PNS region quickly restarts the engine and puts the feedback loop back into operation. This picture is not necessarily contradicted by the observation that the onset of SASI can considerably shift the LESA dipole direction as seen, for example, after 170 ms p.b. in the $27\,M_\odot$ model (bottom right panel in Fig. 3). In fact, if our picture of an outer feedback loop coupled to asymmetric mass accretion is correct, one would expect that massive, large-scale perturbations of the postshock accretion flow like those connected to the onset and presence of violent SASI episodes can lead to a drift of the direction of

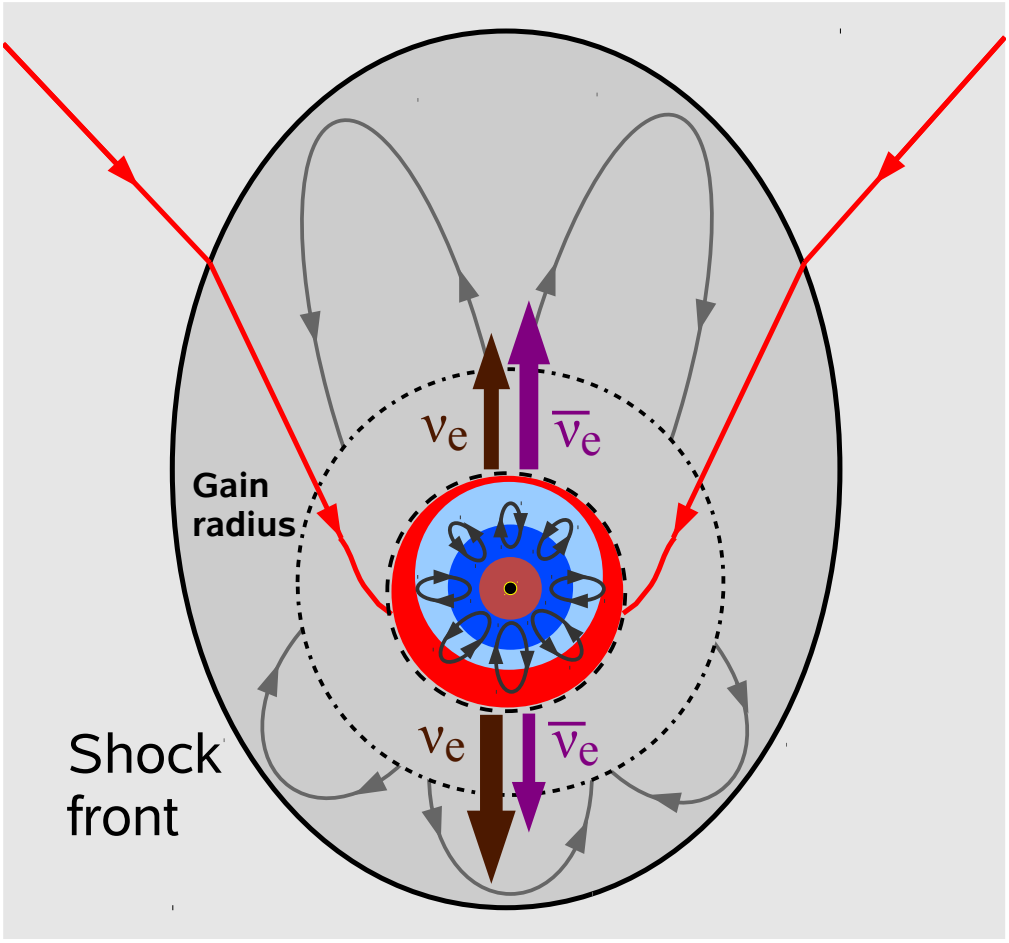

Figure 15. Schematic visualization of the physics components that provide the feedback loop for the self-sustained lepton-emission asymmetry. The outer thick, solid black line indicates the accretion shock, whose dipolar deformation is strongly exaggerated. The dotted circular line marks the gain radius and the inner dashed circular line the neutrinospheres close to the surface of the PNS. Inside the PNS, the bright-red and inner dark-red circular regions indicate the spherical density distribution around the mass center (small, black dot), whereas the displaced, blue circular shapes indicate schematically the deformation of the Y_e distribution (see Fig. 11). The black elliptical loops interior to the neutrinospheres visualize convection inside the PNS, whereas the light gray loops visualize convective overturn between gain radius and shock. PNS convection is stronger in the lower hemisphere (cf. Fig. 9), whereas gain-region convection is more powerful on the opposite side. The red lines mark accretion-stream lines, which are deflected by the deformed shock front. The brown and magenta arrows show the hemispheric asymmetry of the ν_e and $\bar{\nu}_e$ energy fluxes. Note that the sum of the fluxes is nearly isotropic, showing only a percent-level dipole variation, whereas the hemispheric differences of the ν_e and $\bar{\nu}_e$ number and energy fluxes can reach 20–30% of their average values (cf. Figs. 5 and 6). While the convective overturn in the neutrino-heating layer fluctuates strongly in time, the asymmetry of the lepton-number distribution in the PNS mantle layer and the corresponding anisotropic lepton-number emission as well as the deformation of the accretion shock can be stable for hundreds of milliseconds.

the lepton-emission dipole. Similarly, it does not appear astonishing that vigorous, strongly time-dependent convective overturn activity in the neutrino-heating layer creates stochastic variations and fluctuations that can be strong enough to induce a gradual, slow movement of the LESA dipole on secular timescales.

How long can the PNS memory effect last? The life time of the Y_e asymmetry in the PNS depends on two competing effects, on the one hand the inflow of fresh electron number in the asymmetric accretion flow and caused by convective transport out of the high-density PNS core, and on the other hand the loss of lepton number by the anisotropic lepton fluxes, which strive for destroying the hemispheric Y_e asymmetry. The temporal decay of this asymmetry in the PNS mantle can therefore be approximately described by the following differential equation:

$$\frac{1}{2\,m_\mathrm{u}}\,\frac{\mathrm{d}\,(\Delta Y_e M_\mathrm{shell})}{\mathrm{d}t} = \frac{1}{m_\mathrm{u}}\left[\Delta\dot{M}\,\Delta Y_e + \left(\frac{\delta(MY_e)}{\delta t}\right)_\mathrm{mix}\right] - \Delta N\,, \tag{5}$$

where ΔY_e is the difference of the electron fraction in the two hemispheres within a shell of mass M_shell, $\Delta\dot{M}$ is the mass-accretion rate difference (which we assume to carry an excess lepton fraction of ΔY_e into the PNS mantle, $[\delta(MY_e)/\delta t]_\mathrm{mix}$ is the rate of electron-number change associated with enhanced convective mixing, ΔN the neutrino-lepton flux difference between both hemispheres, and m_u the baryon mass. Equation (5) yields a rough estimate of the decay timescale:

$$t_\mathrm{decay} \sim \frac{0.5\,\Delta Y_e M_\mathrm{shell}}{m_\mathrm{u}\Delta N}\,. \tag{6}$$

In this expression we have ignored the positive contributions on the rhs of Eq. (5) because the first term turns out to be subdominant when numbers from the 11.2 $M_\odot$ simulation ($\Delta Y_e \sim 0.05$, $\Delta\dot{M} \sim 0.05\,M_\odot\,\mathrm{s}^{-1}$, cf. Figs. 11 and 12) are used, and the second term is difficult to calculate without digging into the details of the dynamic interaction between the PNS convection and the impact of accretion flows on the PNS. In any case, the inflow of fresh lepton number associated with the positive

source term can only stretch the decay timescale so that our estimate provides a firm lower limit. With numbers deduced from our analysis of the 11.2 $M_\odot$ model, $M_{\rm shell} \sim 0.4\,M_\odot$, $\Delta Y_e \sim 0.05$ (Fig. 11), and $\Delta N \sim 12 \times 10^{55}\,{\rm s}^{-1}$ (Fig. 9), we obtain $t_{\rm decay} \sim 100$ ms. Therefore, once the lepton-emission dipole has developed to its full strength, it will continue to exist for at least 100 ms even if the asymmetries of accretion and PNS convection disappear.

6. SUMMARY AND OUTLOOK

In this paper we have described a new type of nonradial deformation mode that we discovered in our 3D stellar core-collapse simulations using energy-dependent, three-flavor neutrino transport, applied to progenitor stars of 11.2, 20, and 27 $M_\odot$. During the first 100–150 ms of postbounce evolution, a long-lasting, only slowly evolving dipolar neutrino-emission asymmetry establishes itself. It persists throughout the postbounce accretion phase of the stalled SN shock for hundreds of ms, even in those models that show violent SASI activity for parts of their postbounce evolution. This multi-dimensional phenomenon has not been identified unambiguously in any previous 2D simulation. We call the new phenomenon LESA for "Lepton-number Emission Self-sustained Asymmetry." LESA emerges from an instability, i.e., the spherically symmetric state is not stable and the asymmetry grows from any perturbation, no matter how small. In contrast to convection or SASI, the nature of LESA is not simply hydrodynamical, but rather a neutrino-hydrodynamical instability and as such the first of its kind identified in the SN context.

The dipole mode manifests itself most conspicuously in the lepton-number flux (ν_e minus $\bar\nu_e$), whose dipole amplitude can reach 100% of its 4π directional average, i.e., in one direction the lepton-number flux can exceed twice the average, in the opposite direction it can be even somewhat negative ($\bar\nu_e$ number flux exceeds that of ν_e). While dipole amplitudes of the individual ν_e and $\bar\nu_e$ number and energy fluxes of 10–20% can be observed in our 3D calculations of the 11.2 $M_\odot$ progenitor (and somewhat smaller ones in the 27 $M_\odot$ model), heavy-lepton neutrinos as well as the sum of ν_e and $\bar\nu_e$ exhibit only percent-level dipolar luminosity asymmetries.

The neutrino-emission dipole originates from a hemispheric asymmetry of the electron distribution in the mantle layer of the PNS interior to the neutrinospheres, although the density stratification is perfectly spherical and concentric in these regions of extreme gravitational field strength. In the hemisphere of higher ν_e flux, convection in the deeper layers of the PNS mantle is enhanced compared to the opposite side and dredges up electrons more efficiently from the dense, lepton-rich central core. These electrons are mixed outward towards the neutrinospheres and lead to less deleptonized conditions in one hemisphere, supporting the higher ν_e flux. The convective activity seems to be instigated and fostered by shear flows, turbulent motions, and gravity waves caused by the violent impacts of accretion streams in the neutrinospheric region. This connection is suggested by the observed correlation between PNS-convection asymmetry and a considerable asymmetry of the mass-accretion flow, which is stronger in the hemisphere of enhanced PNS convection. The accretion asymmetry also contributes to the lepton-number emission dipole, because the accretion streams carry electron-rich matter and thus supply the PNS with fresh lepton number, but this effect is subdominant.

The global accretion asymmetry is maintained by anisotropic neutrino heating in the gain layer behind the stalled SN shock, because $\bar\nu_e$ leave the neutrinosphere with higher mean energy than ν_e. Therefore, neutrino heating is stronger on the side of lower lepton-number flux, despite the nearly isotropic energy flux of ν_e plus $\bar\nu_e$. Stronger neutrino heating enhances convective overturn in the postshock layer, pushes the shock to a larger stagnation radius and thus produces a dipolar deformation of the shock surface. This shock deformation in turn deflects the accretion flow falling through the shock and, in the time-averaged sense, amplifies the accretion flux to the hemisphere of the PNS facing away from the greater shock radius (Fig. 15).

Anisotropic neutrino heating therefore establishes a feedback mechanism between the neutrino-emission asymmetry on one side and shock deformation and accretion asymmetry on the other. It thus mediates a complex, mutual dependence between lepton-number transport by neutrino fluxes and convection inside the PNS on the one hand and anisotropic convective overturn in the gain layer on the other. This feedback, which involves neutrinos as crucial players, allows the global dipolar asymmetry to become a self-sustained phenomenon, which exists in stable conditions over many dynamical timescales despite the presence of vigorous and highly time-dependent convective overturn in the postshock region and even through phases of violent SASI activity. Stochastic fluctuations of this convective overturn or of the convection in the PNS mantle are probably responsible for initiating the development of the hemispheric asymmetry. The convective SN core seems to be generically unstable against such a dipolar mode of asymmetry. LESA and SASI are independent phenomena, but the latter can influence the former in a complex manner, depending on the relative orientations of the associated vector directions.

LESA could have important implications for a variety of physical processes in the SN core, most importantly nucleosynthesis in the neutrino-heated ejecta, and potentially NS kicks and neutrino-flavor conversion.

Concerning nucleosynthesis, we recall that charged-current reactions of ν_e and $\bar\nu_e$ with neutrons and protons do not only heat the SN blast wave but also set the n/p ratio in the neutrino-driven outflow and thus determine the nucleosynthesis conditions in the innermost SN ejecta. Since ν_e absorption converts neutrons to protons while $\bar\nu_e$ captured on protons create neutrons, the exposure to a higher flux of $\bar\nu_e$ tends to neutronize the expelled matter. The lepton-number emission asymmetry could persist until the explosion sets in or even beyond, fuelled by continued anisotropic PNS convection and/or asymmetric accretion beyond the onset of the explosion. In this case a considerable hemispheric asymmetry of the electron fraction in the ejecta could be expected with possibly favorable conditions for neutron-rich material in the direction where the $\bar\nu_e$ flux has its emission maximum. We speculate that the O-Ne-Mg core explosion of Wanajo, Janka, & Müller (2011), where convective overturn but not SASI played a role, may be a case where we have encountered consequences of the dipolar lepton-emission asymmetry in a 2D model. The moderate hemispheric differences of Y_e in the early neutrino-driven wind (with variations in the range $0.40 \lesssim Y_e \lesssim 0.54$) in this simulation might give an impression of the corresponding effects that could be obtained in future 3D explosions.

Asymmetric neutrino emission imparts a recoil on the nascent NS. We assume a dipolar emission anisotropy of the total neutrino-energy loss rate (the summed contributions of ν

and $\bar{\nu}$ of all flavors),

$$\frac{\mathrm{d}\dot{E}_{\mathrm{tot}}}{\mathrm{d}\Omega} = \frac{\dot{E}_{\mathrm{tot}}}{4\pi}\,(1+\alpha\,\cos\vartheta)\;, \tag{7}$$

where α is the dipole amplitude and ϑ the zenith angle relative to the dipole direction. In this case the NS acceleration is

$$a_{\mathrm{NS}} = \frac{1}{M_{\mathrm{NS}}c}\int_{4\pi}\mathrm{d}\Omega\,\frac{\mathrm{d}\dot{E}_{\mathrm{tot}}}{\mathrm{d}\Omega}\,\cos\vartheta = \frac{\alpha}{3\,c}\,\frac{\dot{E}_{\mathrm{tot}}}{M_{\mathrm{NS}}}\,. \tag{8}$$

With $\dot{E}_{53} \equiv \dot{E}_{\mathrm{tot}}/(10^{53}\,\mathrm{erg\,s^{-1}})$ and $M_{1.5} \equiv M_{\mathrm{NS}}/(1.5\,M_\odot)$ we obtain

$$a_{\mathrm{NS}} \approx 37\,\frac{\alpha}{0.01}\,\frac{\dot{E}_{53}}{M_{1.5}}\;\mathrm{km\,s^{-2}}\,. \tag{9}$$

If $\alpha \sim 0.01$–0.02 and the duration of the emission asymmetry lasts only some hundred milliseconds, corresponding to the duration of the accretion phase, the recoil velocity will not exceed several $10\,\mathrm{km\,s^{-1}}$, depending on the time-integrated neutrino-energy release E_{tot}. But the NS kick velocity could reach 100–200 $\mathrm{km\,s^{-1}}$ for a canonical value of 3×10^{53} erg for the NS gravitational binding energy, if the neutrino-emission dipole continues to exist for the whole period of PNS neutrino cooling. With the luminosity maximum coinciding with the $\bar{\nu}_e$ emission peak in our 3D simulations, the NS acceleration will point in the direction of the strongest ν_e emission. Even in the optimistic (and highly speculative) case that the neutrino-emission dipole survives for seconds, however, the estimated recoil velocity is dwarfed by those that can typically be expected from the "gravitational tug-boat mechanism" associated with the anisotropic ejection of matter in 3D simulations of SN explosions (Wongwathanarat, Janka, & Müller 2010, 2013).

Another small but amusing mechanical consequence of LESA is an angular momentum transfer, i.e., a spin-up of the nascent NS. Weak interactions violate parity maximally, implying that a relativistic ν_e has negative helicity and carries the spin angular momentum $-\hbar/2$ relative to its direction of motion, whereas a $\bar{\nu}_e$ has positive helicity and carries $+\hbar/2$. We denote the lepton-number flux dipole amplitude with A_{Dipole}, i.e., the quantity plotted in Fig. 3. The angular momentum transfer rate then has the magnitude

$$\dot{J} = \frac{\hbar}{2}\,\frac{A_{\mathrm{Dipole}}}{3}\,, \tag{10}$$

because our normalization of the dipole amplitude implies that it is three times the total lepton-number flux projected on the dipole direction. With a typical value $A_{\mathrm{Dipole}} = 3\times10^{56}\;\mathrm{s^{-1}}$ and recalling that $\hbar = 1.054\times10^{-27}\,\mathrm{cm^2\,g\,s^{-1}}$ we find a typical angular-momentum transfer rate of $\dot{J} = 5\times10^{28}\,\mathrm{cm^2\,g\,s^{-2}}$. We recall that the moment of inertia of a homogeneous sphere with mass M and radius R is $I = 2MR^2/5$ and its angular momentum is $J = I\,2\pi f$ with f the rotation frequency. Using as benchmark values $M = 1.5\,M_\odot$ and $R = 15\,\mathrm{km}$, a typical PNS spin-up rate is of the order of $\dot{f} \sim 3\times10^{-18}\,\mathrm{Hz\,s^{-1}}$, a very small value indeed. A much larger effect, however, is non-radial neutrino emission that can transfer orbital angular momentum and cause a spin-down of a rotating NS as first shown by Mikaelian (1977) and Epstein (1978).

Our entire study has ignored neutrino flavor conversion. The LESA phenomenon depends on a subtle hemispheric asymmetry of neutrino heating rates. Certainly this effect would be modified if the ν_e and $\bar{\nu}_e$ fluxes would partially swap flavor with ν_x and $\bar{\nu}_x$ which have different spectral properties and different number fluxes. Moreover, flavor conversion also modifies the neutrino influence on the n/p ratio in the context of nucleosynthesis as first pointed out by Qian et al. (1993) and Qian & Fuller (1995).

The thorniest problem in the context of neutrino flavor conversion is the role of neutrino-neutrino refraction, which causes many complications because of the feedback of flavor conversion on itself (Duan, Fuller & Qian 2010). The justification for ignoring flavor conversion in the dense region below the stalled shock wave is the so-called multi-angle matter effect, which tends to suppress self-induced flavor conversion (Esteban-Pretel et al. 2008; Sarikas et al. 2012; Raffelt, Sarikas & de Sousa Seixas 2013; Chakraborty et al. 2011; Saviano et al. 2012; Chakraborty et al. 2014). In particular, Dasgupta, O'Connor & Ott (2012) have studied the onset of self-induced flavor conversion in a somewhat simplified 3D model. These authors conclude that flavor conversion always begins outside the shock wave.

It is conceivable, however, that these conclusions must be modified in the LESA context, notably in those directions where the lepton number flux is small. The asymmetry between the ν_e and $\bar{\nu}_e$ number fluxes, sometimes denoted with the parameter ϵ, is a crucial ingredient for the stability of the neutrino flux in flavor space (Esteban-Pretel et al. 2007). Moreover, the LESA phenomenon also modifies the electron-density profile which defines the matter effect for neutrino flavor oscillations. Therefore, it remains to be verified that flavor conversion is indeed irrelevant for the LESA phenomenon.

The observations reported in this paper raise many interesting questions. It is obvious that the LESA phenomenon needs much more work and analysis to develop a full understanding, especially concerning how asymmetric PNS convection is stimulated by asymmetric mass accretion and how SASI and LESA interact. Many of our explanations remain tentative and require further confirmation.

In particular, further studies are necessary to reveal how generic the lepton-number emission dipole is. How exactly does its amplification work, what is the underlying mechanism? What is the role of the PNS contraction in this context, and, if it is important, how sensitive is the phenomenon to the nuclear equation of state and the neutrino opacities? How big is the saturation amplitude of LESA and what does it depend on? Could its amplitude be larger than in our present 3D simulations and could its dipolar neutrino-heating asymmetry affect the onset of neutrino-driven SN explosions? How long does LESA last? Does LESA require the inner engine of hemispherically asymmetric PNS convection as a necessary ingredient, or is the role of PNS convection only that of an amplifier of the lepton-number flux asymmetry and that of a stabilizing factor which enables long-term memory? A feedback loop seems possible that is solely based on the outer engine, in which the asymmetric accretion and lepton-number emission on the one hand is intertwined with the dipolar neutrino-heating asymmetry and shock deformation on the other. Answers to these questions are indispensable to reach firm conclusions on the importance of LESA for NS kicks, the explosion mechanism and asymmetries, and SN nucleosynthesis.

Linear growth studies would help to develop deeper insights. It would be especially useful to construct toy models that capture the essential parts of the mechanism but reduce its complexity and thus allow a better control of the interplay of its different components. Such studies would be particularly useful because numerical models are always prone to ar-

tifacts. For example, it is unclear whether our findings are affected by approximations involved in our treatment, e.g., the ray-by-ray-plus transport, which does not include nonradial neutrino fluxes, the use of a monopole description of the gravitational potential, or the spherical core of 10 km radius, which fixes the PNS to its location at the grid center. It is therefore essential that other groups investigate their neutrino-hydrodynamics simulations for hints of effects similar to our LESA phenomenon.

Note added. After our work had been circulated in preprint form, the authors of Couch & O'Connor (2014) informed us that they also found LESA features in their 3D models. On the other hand, Dolence, Burrows, & Zhang (2014) do not find any evidence for LESA in their 2D simulations (see their Fig. 11, where they plot the evolution of the dipole-to-monopole ratio for the lepton-number flux). Performing a similar analysis for our own 2D models, we do find a strong LESA effect, commensurate with our 3D findings. However, in 2D we see an oscillatory, high-amplitude lepton-flux asymmetry, which can change its north-south orientation on timescales of order 10 ms. This behavior differs from typical features of LESA in 3D, like its persistence and directional stability, and asymmetric accretion and heating are difficult to diagnose in such a strongly time-variable situation. While a more detailed future study of our 2D models may shed more light on this question, we conclude that the appearance or not of LESA is not directly related to the dimensionality of the simulation.

One difference between our works is that we treat neutrino transport in the ray-by-ray-plus approximation, an approach also used by Couch & O'Connor (2014), whereas Dolence, Burrows, & Zhang (2014) use a multi-dimensional flux-limited diffusion scheme, leading them to speculate that LESA is an artifact of the ray-by-ray technique. We note, however, that there are numerous other differences, including neutrino interaction rates, and that our 2D models have rather different physical characteristics at comparable epochs, in particular differ strongly in the evolution of the shock radius and actually explode. Understanding the differences in these results requires a systematic study of the influence of all physics inputs and their numerical representation. The ray-by-ray approximation ignores lateral radiative neutrino transport, although it includes, of course, advective transport of neutrinos trapped in the stellar medium (see Buras et al. 2006b). It seems rather implausible that lateral radiative diffusion, caused by relatively weak transverse gradients in the PNS, could suppress a global dipole asymmetry that would otherwise occur. Similarly, it is difficult to imagine that the accretion and lepton-emission asymmetries on the largest possible (hemispheric) scale could be wiped out by angular smoothing of the neutrino heating in the gain layer on much smaller scales (cf. Sumiyoshi et al. 2014). Such findings would be intriguing in their own right. In any case, a satisfactory answer to this question depends on a true physical understanding of the LESA phenomenon and on observing it in simulations where the neutrino treatment does not have the shortcomings of the ray-by-ray-plus approximation.

ACKNOWLEDGEMENTS

We are grateful to Ewald Müller for discussions. This research was supported by the Deutsche Forschungsgemeinschaft through the Transregional Collaborative Research Center SFB/TR 7 "Gravitational Wave Astronomy" and the Cluster of Excellence EXC 153 "Origin and Structure of the Universe" (http://www.universe-cluster.de) and by the EU through ERC-AdG No. 341157-COCO2CASA. I.T. acknowledges partial support from the Netherlands Organization for Scientific Research (NWO). The results described in this paper could only be achieved with the assistance of high performance computing resources (Tier-0) provided by PRACE on CURIE TN (GENCI@CEA, France) and SuperMUC (GCS@LRZ, Germany). We also thank the Rechenzentrum Garching for computing time on the IBM iDataPlex system *hydra*.

REFERENCES

Bethe, H. A. 1990, Rev. Mod. Phys., 62, 801
Blondin, J. M., Mezzacappa, A., & DeMarino, C. 2003, ApJ, 584, 971
Blondin, J. M. & Mezzacappa, A. 2006, ApJ, 642, 401
Blondin, J. M. & Mezzacappa, A. 2007, Nature, 445, 58
Blondin, J. M. & Shaw, S. 2007, ApJ, 656, 366
Buras, R., Janka, H.-Th., Keil, M., Raffelt, G. G., & Rampp, M. 2003 ApJ, 587, 320
Buras, R., Janka, H.-T., Rampp, M., & Kifonidis, K. 2006a, A&A, 457, 281
Buras, R., Rampp, M., Janka, H.-T., & Kifonidis, K. 2006b, A&A, 447, 1049
Burrows, A. & Fryxell, B. A. 1992, Science, 258, 430
Burrows, A., Hayes, J., & Fryxell, B. A. 1995, ApJ, 450, 830
Burrows, A. & Lattimer, J. M. 1988, Phys. Rep., 163, 51
Chakraborty, S., Fischer, T., Mirizzi, A., Saviano, N., & Tomàs, R. 2011, Phys. Rev. Lett., 107, 151101
Chakraborty, S., Mirizzi, A., Saviano, N., & de Sousa Seixas, D. 2014, Phys. Rev. D, 89, 093001
Colella, P., & Woodward, P. R. 1984, J. Comp. Phys., 54, 174
Couch, S. M. 2013, ApJ, 775, 35
Couch, S. M. & O'Connor, E. P. 2014, ApJ, 785, 123
Dessart, L., Burrows, A., Livne, E., & Ott, C. D. 2006, ApJ, 645, 534
Dolence, J. C., Burrows, A., Murphy, J. W., & Nordhaus, J. 2013, ApJ, 765, 110
Dolence, J. C., Burrows, A., & Zhang, W. 2014, arXiv:1403.6115
Dasgupta, B., O'Connor, E. P., & Ott, C. D. 2012, Phys. Rev. D, 85, 065008
Duan, H., Fuller, G. M., & Qian, Y.-Z. 2010, Ann. Rev. Nucl. Part. Sci., 60, 569
Epstein, R. 1978, ApJ, 219, L39
Epstein, R. 1979, MNRAS, 188, 305
Esteban-Pretel, A., Pastor, S., Tomàs, R., Raffelt, G. G., & Sigl, G. 2007 Phys. Rev. D, 76, 125018
Esteban-Pretel, A., et al. 2008, Phys. Rev. D, 78, 085012
Fernández, R. 2010, ApJ, 725, 1563
Foglizzo, T. 2002, A&A, 392, 353
Foglizzo, T., Galletti, P., Scheck, L., & Janka, H.-Th. 2008, ApJ, 654, 1006
Foglizzo, T., Scheck, L., & Janka, H.-Th. 2006, ApJ, 652, 1436
Foglizzo, T., Masset, F., Guilet, J., & Durand, G. 2012, Phys. Rev. Lett., 108, 051103
Fryer, C. L. & Warren, M. S., 2002, ApJ, 574, L65
Fryer, C. L. & Warren, M. S., 2004, ApJ, 601, 391
Fryxell, B. A., Müller, E., & Arnett, D. 1989, Max-Planck-Institut für Astrophysik, Preprint Nr. 449
Guilet, J. & Fernández, R. 2013, arXiv:1310.2616
Guilet, J. & Foglizzo, T. 2012, MNRAS, 421, 546
Hanke, F., Marek, A., Müller, B., & Janka, H.-Th. 2012, ApJ, 755, 138
Hanke, F., Müller, B., Wongwathanarat, A., Marek, A., & Janka, H.-Th. 2013, ApJ, 770, 66
Herant, M., Benz, W., & Colgate, S. 1992, ApJ, 395, 642
Herant, M., Benz, W., Hix, W. R., Fryer, C.L., & Colgate, S. A. 1994, ApJ, 435, 339
Iwakami, W., Kotake, K., Ohnishi, N., Yamada, S., & Sawada, K. 2008, ApJ, 678, 1207
Iwakami, W., Ohnishi, N., Kotake, K., Yamada, S., & Sawada, K. 2009, Ap&SS, 322, 43
Janka, H.-Th. 2001, A&A, 368, 527
Janka, H.-Th., Buras, R., Kifonidis, K., Plewa, T., & Rampp, M. 2003, in: From Twilight to Highlight: The Physics of Supernovae, Eds. W. Hillebrandt & B. Leibundgut, Springer, Berlin, p. 39
Janka, H.-Th., Buras, R., Kifonidis, K., Rampp, M., & Plewa, T. 2004, in: Stellar Collapse, Ed. C. L. Fryer, Kluwer, Dordrecht, p. 65

Janka, H.-Th., Hanke, F., Hüdepohl, L., Marek, A., Müller, B. & Obergaulinger, M. 2012, PTEP 2012, 01A309
Janka, H.-Th. & Müller, E. 1993, in: Frontiers of Neutrino Astrophysics, Eds. Y. Suzuki & K. Nakamura, p. 203
Janka, H.-Th. & Müller, E. 1995, ApJ, 448, L109
Janka, H.-Th. & Müller, E. 1996, A&A, 306, L167
Keil, W., Janka, H.-Th., & Müller, E. 1996, ApJ, 473, L111
Keil, M., Raffelt, G. G., & Janka, H.-Th. 2003, ApJ, 590, 971
Lattimer, J. M., & Swesty, F. D. 1991, Nucl. Phys. A, 535, 331
Lund, T., Marek, A., Lunardini, C., Janka, H-Th., Raffelt, G. 2010, Phys. Rev. D, 82, 063007
Marek, A. & Janka, H. 2009, ApJ, 694, 664
Marek, A., Janka, H-Th., & Müller, E. 2009, A&A, 496, 475
Marek, A., Dimmelmeier, H., Janka, H.-T., Müller, E., & Buras, R. 2006, A&A, 445, 273
Mezzacappa, A., Calder, A. C., Bruenn, S. W., Blondin, J. M., Guidry, M. W., Strayer, M. R., & Umar, A. S. 1998, ApJ, 495, 911
Mikaelian, K. O. 1977, ApJ, 214, L23
Miller, D. S., Wilson, J. R., & Mayle, R. W. 1993, ApJ, 415, 278
Müller, B., Janka, H.-T., & Marek, A. 2012a, ApJ, 756, 84
Müller, B., Janka, H.-T., & Heger, A. 2012b, ApJ, 761, 72
Müller, B., Janka, H.-Th., & Marek, A. 2013, ApJ, 766, 43
Müller, E. & Janka, H.-Th. 1994, in: Reviews in Modern Astronomy, 7, Ed. G. Klare, Astronomische Gesellschaft, Hamburg, p. 103
Müller, E. & Janka, H.-Th. 1997, A&A, 317, 140
Müller, E., Janka, H.-Th., & Wongwathanarat, A. 2012, A&A, 537, A63
Murphy, J. W. & Burrows, A. 2008, ApJ, 688, 1159
Murphy, J. W., Ott, C. D., & Burrows, A. 2009, ApJ, 707, 1173
Nordhaus, J., Burrows, A., Almgren, A., & Bell, J. 2010, ApJ, 720, 694
Nordhaus, J., Brandt, T. D., Burrows, A., Livne, E., & Ott, C. D. 2010, Phys. Rev. D, 82, 103016
Nordhaus, J., Brandt, T. D., Burrows, A., & Almgren, A. 2012, MNRAS, 423, 1805
Qian, Y.-Z. & Fuller, G. M. 1995, Phys. Rev. D, 52, 656
Qian, Y.-Z., Fuller, G. M., Mathews, G. J., Mayle, R. W., Wilson, J. R., & Woosley, S. E. 1993, Phys. Rev. Lett., 71, 1965
Raffelt, G. G. 2001, ApJ, 561, 890
Raffelt, G. G., Sarikas, S., & de Sousa Seixas, D. 2013, Phys. Rev. Lett., 111, 091101
Rampp, M., & Janka, H.-T. 2002, A&A, 396, 361
Rantsiou, E., Burrows, A., Nordhaus, J., & Almgren, A. 2010, ApJ, 732, 57
Sarikas, S., Raffelt, G. G., Hüdepohl, L., & Janka, H.-T. 2012, Phys. Rev. Lett., 108, 061101
Saviano, N., Chakraborty, S., Fischer, T., & Mirizzi, A. 2012, Phys. Rev. D, 85, 113002
Scheck, L., Plewa, T., Janka, H.-Th., Kifonidis, K., & Müller, E. 2004, Phys. Rev. Lett., 92, 011103
Scheck, L., Kifonidis, K., Janka, H.-Th., & Müller, E. 2006, A&A, 457, 963
Scheck, L., Janka, H.-Th., Foglizzo, T., & Kifonidis, K. 2008, A&A, 477, 931
Sumiyoshi, K., Takiwaki, T., Matsufuru, H., & Yamada, S. 2014, arXiv:1403.4476
Tamborra, I., Hanke, F., Müller, B., Janka, H.-Th., & Raffelt, G. 2013, Phys. Rev. Lett., 111, 121104
Tamborra, I., Raffelt, G., Hanke, F., Janka, H.-Th., & Müller, B. 2014, arXiv:1406.0006
Takiwaki, T., Kotake, K., & Suwa, Y. 2014, ApJ, 786, 83
Wanajo, S., Janka, H.-Th., & Müller, B. 2011, ApJ, 726, L15
Wongwathanarat, A., Janka, H.-Th., & Müller, E. 2010, ApJ, 725, L106
Wongwathanarat, A., Janka, H.-Th., & Müller, E. 2013, A&A, 552, A126
Woosley, S. E. & Heger, A. 2007, PhR, 442, 269
Woosley, S. E., Heger, A., & Weaver, T. A. 2002, Rev. Mod. Phys., 74, 1015
Yamasaki, T. & Foglizzo, T. 2008, ApJ, 679, 607